Scientific Research Publishing

Journal of Applied Mathematics and Physics, 2026, 14(11), 4842-4892
https://www.scirp.org/journal/jamp
ISSN Online: 2327-4379
ISSN Print: 2327-4352

Stationary Branches and Oscillatory Regimes of the Debyaoui-Ersoy Model in a Variable Channel: Hydrostatic Limits, Phase Portraits, and Numerical Investigations

Mehmet Ersoy

Institut de Mathématiques de Toulon (IMATH), Université de Toulon, La Garde, France
Email: ersoy@univ-tln.fr

How to cite this paper: Ersoy, M. (2026) Stationary Branches and Oscillatory Regimes of the Debyaoui-Ersoy Model in a Variable Channel: Hydrostatic Limits, Phase Portraits, and Numerical Investigations. *Journal of Applied Mathematics and Physics*, **14**, 4842-4892.
https://doi.org/10.4236/jamp.2026.1411236

Received: October 14, 2026
Accepted: November 23, 2026
Published: November 26, 2026

Copyright © 2026 by author(s) and Scientific Research Publishing Inc.
This work is licensed under the Creative Commons Attribution International License (CC BY 4.0).
http://creativecommons.org/licenses/by/4.0/

Open Access

Abstract

We investigate stationary hydraulic regimes of the Debyaoui-Ersoy model in a rectangular channel with variable width and bottom topography. The hydrostatic analysis classifies globally smooth branches and the controlled family of entropy-admissible hydraulic jumps. For the Gaussian channel, the downstream depth determines a unique jump position within that family. For the continuous dispersive problem with prescribed endpoint slopes, we prove local existence near a uniform subcritical flow under a non-resonance condition at fixed positive dispersion. The hydrostatic-limit theorems concern existing uniformly positive and bounded families with the stated compactness and regime assumptions. They identify smooth limits and give a quadratic error estimate under uniform subcritical regularity. A dissipative hydrostatic jump cannot be a strong limit of such stationary inviscid dispersive families. We also derive necessary averaged balances for subsequential oscillatory limits and an explicit Young measure for exact periodic solutions in a constant channel. Continuous collocation illustrates the slope boundary problem. A separate finite-volume study uses exterior-state boundary data and the original Gaussian geometry. Its portraits describe discrete branches selected by the stated continuation procedure. Agreement between direct stationary solution and long-time integration verifies equilibria of the same discrete equations at fixed mesh. Refinement and outlet diagnostics reveal the effects of numerical dissipation and boundary closure; they do not establish convergence to the continuous slope problem or a selected oscillatory limit for hydraulic-jump data.

Keywords

Variable-Width Shallow Water, Serre-Green-Naghdi Model, Hydraulic Jump, Singular Limit, Total Variation, Stationary Finite Volumes

1. Introduction

Stationary free-surface flows in channels with variable width and bottom topography provide a natural setting for studying hydraulic transitions. Depending on the channel geometry, the prescribed discharge and the downstream water depth, the flow may remain subcritical, pass smoothly through a critical state, or undergo a hydraulic jump. The hydrostatic shallow-water equations describe these configurations through the interaction between conservation laws, geometric source terms and boundary conditions. Their stationary solutions also provide useful analytical benchmarks for numerical methods, as illustrated by the collection of test problems in [1]. When non-hydrostatic effects become significant, however, dispersion introduces additional spatial scales and allows oscillatory profiles whose relation to these hydrostatic states requires a separate analysis.

The Serre-Green-Naghdi equations [2] [3] retain the leading dispersive effects of long surface waves while allowing fully nonlinear variations of the water depth. Debyaoui and Ersoy [4] [5] extended this framework to section-averaged descriptions of flows in channels and rivers with variable geometry. The present work investigates the stationary branches of their model in a rectangular channel, with particular attention to the hydrostatic limit, the occurrence of oscillations, and the numerical computation of hydraulic regimes.

Let $x \in I = [x_L, x_R]$ denote the longitudinal coordinate, $\sigma(x) > 0$ the channel width, and $d(x)$ the bottom elevation. The unknowns are the water depth $h(t,x) > 0$ and the section-averaged velocity $u(t,x)$. We write

$$A = \sigma h, \quad Q = Au, \quad \eta = h + d$$

for the wetted area, discharge and free-surface elevation, respectively. With $g > 0$ denoting gravitational acceleration, the rectangular Debyaoui-Ersoy equations considered here take the form

$$\begin{aligned} &\partial_t A + \partial_x Q = 0, \\ &\partial_t Q + \partial_x \left(\frac{Q^2}{A} + \frac{g\sigma h^2}{2} + \mu^2 \sigma \Pi \right) = \frac{g\sigma' h^2}{2} - g\sigma h d' + \mu^2 \left(\sigma' \Pi - \sigma d' P_b \right). \end{aligned} \tag{1.1}$$

Here μ^2 multiplies the non-hydrostatic contributions, Π is the depth-integrated non-hydrostatic pressure, and P_b is its value at the bottom, with pressure normalized by the constant fluid density. The pressure closure is

$$\Pi = \frac{h^3}{3}\mathrm{A} + \frac{h^2}{2}\mathrm{B}, \quad P_b = \frac{h^2}{2}\mathrm{A} + h\mathrm{B}, \tag{1.2}$$

where

$$\begin{aligned} K &= \frac{1}{\sigma}\partial_x(\sigma u), \\ \mathrm{A} &= K^2 - \partial_t K - \frac{u}{\sigma}\partial_x(\sigma K), \\ \mathrm{B} &= \partial_t(ud') + \frac{u}{\sigma}\partial_x(\sigma u d'). \end{aligned} \tag{1.3}$$

These expressions specify the width-weighted closure used in the main analysis. In the notation introduced later, $DI_1 = \sigma\Pi$ and $DI_2 = \sigma'\Pi - \sigma d' P_b$. For constant width and a flat bottom, the system reduces to the classical one-dimensional Serre-Green-Naghdi equations. Setting $\mu = 0$ gives the hydrostatic shallow-water equations in a variable rectangular channel.

For stationary solutions, mass conservation yields $Q \equiv Q_L$. In the hydrostatic case, the hydraulic head

$$\mathcal{B}_Q(x,h) = h + d(x) + \frac{Q_L^2}{2g\sigma(x)^2 h^2} \tag{1.4}$$

is constant along each smooth part of the profile. Its dependence on the depth determines the subcritical and supercritical branches, which meet at the critical level $F^2 = Q_L^2 / \left(g\sigma^2 h^3\right) = 1$. A stationary hydraulic jump connects conjugate states satisfying the mass and momentum conditions, with a strict loss of hydraulic head. For $\mu > 0$, the pressure terms increase the spatial differential order of the stationary problem and introduce the possibility of oscillatory transitions. Understanding how these dispersive branches relate to the hydrostatic classification is the central question of this paper.

The role of oscillations in hydraulic transitions is closely connected to the broader theory of dispersive shock waves and modulation [6]. For the Serre-Green-Naghdi equations, Kalisch, Khorsand and Mitsotakis [7] examined mechanical balance laws and the contribution of oscillations to the energy budget of undular bores. More recently, Bolbot, Mitsotakis and Tzavaras [8] studied a modified Serre-Green-Naghdi system with dissipation and established convergence of travelling waves to shallow-water entropy shocks in a suitable dispersion-diffusion regime. These results emphasize the importance of distinguishing dispersive oscillations from dissipative hydraulic transitions. For the inviscid DE model, this distinction raises precise questions about the compactness of stationary families, the preservation of hydraulic head, and the behaviour of total variation as $\mu \to 0$.

We address these questions by combining an exact hydrostatic description with analytical and numerical investigations of the dispersive problem. We first classify the smooth hydrostatic branches and construct the family of entropy-admissible hydraulic jumps downstream of a geometric control point. For the Gaussian channel considered in the numerical experiments, this gives an explicit portrait in the (Q_L, h_R) plane, where h_R is the prescribed downstream depth. The portrait identifies the critical boundary curves and the range of boundary data admitting a controlled hydraulic jump, whose position is uniquely determined within this family.

We then derive stationary identities and estimates for the dispersive equations. For the continuous boundary problem with prescribed discharge, downstream depth and zero endpoint slopes, we prove local existence near a uniform subcritical flow at fixed non-resonant dispersion. This result concerns small geometric perturbations; the small-dispersion comparison results remain conditional on the existence of families satisfying their explicit depth, compactness and regime as-

sumptions. In the uniformly subcritical case, an additional uniform $W^{3,\infty}$ bound yields an $O\left(\mu^2\right)$ error estimate in $W^{1,\infty}$. For hydraulic-jump configurations, a dissipative hydrostatic jump of nonzero strength cannot be a strong L^1 limit of classical stationary dispersive solutions whose depths remain uniformly bounded above and away from zero. Exact periodic families show that uniform depth convergence can coexist with a nonzero variation defect. Without strong compactness, we obtain necessary Young-measure balances and an explicit constant-channel example, rather than a general selection theory for oscillatory transitions.

The numerical study follows the same three hydraulic configurations: smooth subcritical flow, smooth transcritical flow, and boundary data associated with a hydrostatic hydraulic jump. Continuous collocation approximates the slope boundary problem on a localized geometry. The finite-volume method incorporates hydrostatic reconstruction [9], uses the original Gaussian geometry, and imposes hydraulic data through exterior states. These are two distinct boundary problems. Agreement between directly computed finite-volume equilibria and long-time integration from rest verifies the solution of the same semidiscrete equations at fixed mesh; it does not establish convergence to the continuous slope problem. Parameter portraits describe branches reached by the specified continuation procedure. Boundary diagnostics and refinement assess their dependence on numerical closure and resolution, particularly when oscillatory transitions develop.

The paper is organized as follows. Section 2 presents the hydrostatic classification and the boundary-data portrait. Section 3 develops the dispersive stationary formulation and the numerical solvers. Section 4 establishes the comparison results and analyzes total-variation defects. Section 5 provides continuous numerical illustrations, while Section 6 examines finite-volume profiles, refinement and parameter portraits. Section 7 compares the directly computed equilibria with long-time numerical evolution.

2. Hydrostatic Stationary Solutions and the Boundary-Data Portrait

We first consider the hydrostatic limit $\mu = 0$ of the rectangular Debyaoui-Ersoy Equations (1.1). Let $I = \left[x_L, x_R\right]$, with channel width $\sigma\left(x\right) > 0$ and bottom elevation $d\left(x\right)$. The prescribed boundary data are the inflow discharge $Q_L > 0$ and the downstream depth $h_R > 0$. Writing $A = \sigma h$ and $Q = Au$, the stationary mass and momentum equations are

$$Q' = 0, \quad \left(\frac{Q^2}{\sigma h} + \frac{g\sigma h^2}{2}\right) = \frac{g\sigma' h^2}{2} - g\sigma h d'. \tag{2.1}$$

Thus $Q \equiv Q_L$ throughout the channel. We write $Q = Q_L$ in the remainder of this section.

On every smooth interval where $h > 0$, the momentum equation is equivalent to conservation of the hydraulic head:

$$\mathcal{B}_Q\left(x,h(x)\right)=B,\quad \mathcal{B}_Q\left(x,h\right)=h+d\left(x\right)+\frac{Q^2}{2g\sigma\left(x\right)^2h^2}. \tag{2.2}$$

Indeed, the difference between the left- and right-hand sides of the momentum equation in (2.1) equals $g\sigma h\frac{\mathrm{d}}{\mathrm{d}x}\mathcal{B}_Q\left(x,h(x)\right)$. A stationary profile can therefore be constructed from algebraic depth relations on its smooth portions. Across a hydraulic jump, mass and momentum remain conserved, while the hydraulic head decreases.

2.1. Critical Head and Smooth Stationary Branches

The squared Froude number, critical depth and critical head are

$$\begin{aligned} &F^2\left(x,h\right)=\frac{Q^2}{g\sigma\left(x\right)^2h^3},\quad h_c\left(x;Q\right)=\left(\frac{Q^2}{g\sigma\left(x\right)^2}\right)^{1/3},\\ &B_c\left(x;Q\right)=d\left(x\right)+\frac{3}{2}h_c\left(x;Q\right). \end{aligned} \tag{2.3}$$

At fixed x,

$$\partial_h\mathcal{B}_Q=1-F^2,\quad \partial_{hh}\mathcal{B}_Q=\frac{3Q^2}{g\sigma\left(x\right)^2h^4}>0.$$

The head is therefore strictly decreasing on $\left(0,h_c\right)$ and strictly increasing on $\left(h_c,\infty\right)$, with minimum B_c. Consequently, if $B>B_c\left(x;Q\right)$, the equation $\mathcal{B}_Q\left(x,h\right)=B$ has exactly two positive roots:

$$0<h_-\left(x;B,Q\right)<h_c\left(x;Q\right)<h_+\left(x;B,Q\right). \tag{2.4}$$

The lower root is supercritical and the upper root is subcritical. For $B=B_c$, both roots coincide with h_c; for $B<B_c$, there is no positive root.

Define

$$B_*\left(Q\right)=\max_{x\in I}B_c\left(x;Q\right),\quad x_c\left(Q\right)\in\arg\max_{x\in I}B_c\left(x;Q\right). \tag{2.5}$$

A globally defined constant-head profile requires $B\geq B_*$. When $B>B_*$, both roots in (2.4) extend smoothly across the whole interval. When $B=B_*$, their connection at a critical point determines whether the resulting profile is smooth.

Proposition 2.1 (Smooth passage through a control point). *Assume that σ,d are smooth on I, with $\sigma>0$, and that $B_c\left(\cdot;Q\right)$ has a unique interior maximum x_c satisfying*

$$B_{c''}\left(x_c;Q\right)<0.$$

Assume also that σ,d are analytic near x_c. There are exactly two C^1 positive constant-head profiles that cross the critical level at x_c. Their head is B_*. One is subcritical upstream and supercritical downstream; the other has the opposite orientation. Both are analytic through x_c.

For the subcritical-to-supercritical crossing,

$$h(x)-h_c(x;Q)=-\sqrt{-\frac{h_c(x_c;Q)B_c''(x_c;Q)}{3}}(x-x_c)+O\left((x-x_c)^2\right). \tag{2.6}$$

The sign is reversed for the other crossing. The control point satisfies

$$B_c'(x_c;Q)=0,\quad d'(x_c)=h_c(x_c;Q)\frac{\sigma'(x_c)}{\sigma(x_c)}. \tag{2.7}$$

Proof. At a critical point, the head relation gives $B=B_c(x_c;Q)$. Existence of a positive root throughout I requires $B\geq B_*$, hence $B=B_*$. Moreover,

$$h_{c'}=-\frac{2}{3}h_c\frac{\sigma'}{\sigma},\quad B_c'=d'-h_c\frac{\sigma'}{\sigma},$$

which proves (2.7).

The exact factorization

$$\mathcal{B}_Q(x,h)-B_c(x;Q)=\frac{\left(h-h_c(x;Q)\right)^2\left(2h+h_c(x;Q)\right)}{2h^2} \tag{2.8}$$

shows that the head has a quadratic minimum at the critical depth. Near x_c, write

$$B_*-B_c(x;Q)=(x-x_c)^2\beta(x),\quad \beta(x_c)=-\frac{1}{2}B_c''(x_c;Q)>0.$$

Setting

$$a(x,h)=\frac{2h+h_c(x;Q)}{2h^2},$$

the head equation becomes

$$h-h_c(x;Q)=\pm(x-x_c)\sqrt{\frac{\beta(x)}{a(x,h)}}.$$

The analytic implicit-function theorem provides one analytic solution for each sign. Since $a\left(x_c,h_c(x_c;Q)\right)=3/\left(2h_c(x_c;Q)\right)$, their expansions are given by (2.6) and its opposite.

Choosing the same algebraic root on both sides of x_c instead gives a leading term proportional to $|x-x_c|$. Such a profile has a corner and is not C^1. □

For later use, the left-to-right smooth transcritical profile is written explicitly as

$$h_{\mathrm{tr}}(x;Q)=\begin{cases}h_+(x;B_*,Q), & x<x_c,\\ h_c(x_c;Q), & x=x_c,\\ h_-(x;B_*,Q), & x>x_c.\end{cases} \tag{2.9}$$

Interchanging h_+ and h_- gives the reverse crossing.

At the downstream boundary, introduce

$$H_{\mathrm{sup}}(Q)=h_-\left(x_R;B_*(Q),Q\right),\quad H_{\mathrm{sub}}(Q)=h_+\left(x_R;B_*(Q),Q\right). \tag{2.10}$$

Under the assumptions of Proposition 2.1,

$$H_{\mathrm{sup}}(Q)<h_c(x_R;Q)<H_{\mathrm{sub}}(Q).$$

The head associated with a prescribed downstream depth is

$$B_R(Q,h_R)=\mathcal{B}_Q(x_R,h_R).$$

The monotonicity of $\mathcal{B}_Q(x_R,\cdot)$ on either side of the critical depth yields the following classification of globally C^1 positive profiles:

$$\begin{array}{l|l} 0<h_R<H_{\sup} & \text{globally supercritical,} \\ h_R=H_{\sup} & \text{smooth subcritical-to-supercritical crossing,} \\ H_{\sup}<h_R<H_{\sub} & \text{no globally smooth positive profile,} \\ h_R=H_{\sub} & \text{smooth supercritical-to-subcritical crossing,} \\ h_R>H_{\sub} & \text{globally subcritical.} \end{array} \tag{2.11}$$

For the globally subcritical and supercritical cases, $B=B_R>B_*$. On the two transition curves, $B=B_*$. This classification concerns stationary profiles; their selection by an evolution problem also depends on the boundary conditions imposed on that problem.

2.2. The Controlled Hydraulic-Jump Family

We now consider a flow that first follows (2.9) and then undergoes a hydraulic jump at some $x_s\in(x_c,x_R)$. The upstream head is therefore fixed at $B^-=B_*$.

Since the geometry is continuous at x_s, the stationary Rankine-Hugoniot conditions require continuity of discharge and momentum flux. Writing

$$q_s=\frac{Q}{\sigma(x_s)},\quad h_s^-=h_-(x_s;B_*,Q),$$

the momentum condition is

$$\frac{q_s^2}{h_s^-}+\frac{g\left(h_s^-\right)^2}{2}=\frac{q_s^2}{h_s^+}+\frac{g\left(h_s^+\right)^2}{2}. \tag{2.12}$$

Apart from the trivial solution $h_s^+=h_s^-$, it gives the conjugate depth

$$F_-^2=\frac{q_s^2}{g\left(h_s^-\right)^3},\quad h_s^+=\frac{h_s^-}{2}\left(\sqrt{1+8F_-^2}-1\right). \tag{2.13}$$

Because h_s^- is supercritical, $h_s^+>h_s^-$ and the downstream state is subcritical. The downstream head and head loss are

$$B^+(Q,x_s)=\mathcal{B}_Q(x_s,h_s^+),\quad B_*-B^+(Q,x_s)=\frac{\left(h_s^+-h_s^-\right)^3}{4h_s^-h_s^+}>0. \tag{2.14}$$

Thus the jump satisfies the stationary mechanical entropy inequality

$$gQ\left(B^+-B^-\right)<0.$$

Beyond the jump, the depth is obtained from the subcritical root with head $B^+(Q,x_s)$. A strictly subcritical downstream continuation exists provided

$$B^+(Q,x_s)>\max_{x\in[x_s,x_R]}B_c(x;Q).$$

Its downstream boundary value defines the shooting map

$$J_Q(x_s)=h_+\left(x_R;B^+(Q,x_s),Q\right). \tag{2.15}$$

The prescribed boundary condition is satisfied when $J_Q(x_s)=h_R$.

Lemma 2.2 (Variation of the downstream head). *Let* $q(x)=Q/\sigma(x)$. *Along the conjugate states defined above*,

$$\frac{\mathrm{d}B^{+}}{\mathrm{d}x_s}=\frac{h_s^{+}-h_s^{-}}{h_s^{+}}\left[d'(x_s)+\frac{q_s q_s'}{g h_s^{-} h_s^{+}}\right]=\frac{h_s^{+}-h_s^{-}}{h_s^{+}}\left[d'(x_s)-\frac{q_s^2\sigma'(x_s)}{g\sigma(x_s)h_s^{-}h_s^{+}}\right]. \tag{2.16}$$

Proof. Set

$$B(h,q,d)=h+d+\frac{q^2}{2gh^2},\quad M(h,q)=\frac{q^2}{h}+\frac{gh^2}{2}.$$

The upstream head is constant and the momentum fluxes agree:

$$B\left(h_s^{-},q_s,d(x_s)\right)=B_{*},\quad M\left(h_s^{-},q_s\right)=M\left(h_s^{+},q_s\right).$$

Using $M_h=ghB_h$ and $M_q=2q/h$, differentiation gives

$$B_h\left(h_s^{-}\right)\left(h_s^{-}\right)'=-d'(x_s)-\frac{q_s q_s'}{g\left(h_s^{-}\right)^2},$$

and

$$h_s^{+}B_h\left(h_s^{+}\right)\left(h_s^{+}\right)'=h_s^{-}B_h\left(h_s^{-}\right)\left(h_s^{-}\right)'+\frac{2q_s q_s'}{g}\left(\frac{1}{h_s^{-}}-\frac{1}{h_s^{+}}\right).$$

Substitution into

$$\left(B^{+}\right)'=B_h\left(h_s^{+}\right)\left(h_s^{+}\right)'+d'(x_s)+\frac{q_s q_s'}{g\left(h_s^{+}\right)^2}$$

yields the first identity. The second follows from $q_s'=-q_s\sigma'(x_s)/\sigma(x_s)$. □

Whenever the downstream state remains subcritical, implicit differentiation of (2.15) gives

$$J_Q'(x_s)=\frac{\left(B^{+}\right)'(Q,x_s)}{1-\dfrac{Q^2}{g\sigma(x_R)^2J_Q(x_s)^3}}. \tag{2.17}$$

The denominator is positive. Hence the downstream head and the shooting map have the same monotonicity.

2.3. The Boundary-Data Portrait for the Gaussian Channel

We consider the channel

$$\begin{aligned}&x_L=0,\quad x_R=60,\quad g=9.81,\\&\sigma(x)=1-0.25\mathrm{e}^{-((x-25)/7)^2},\quad d(x)=0.15\mathrm{e}^{-((x-25)/6)^2}.\end{aligned} \tag{2.18}$$

The bottom rises and the channel contracts on $(0,25)$, where $d'>0$ and $\sigma'<0$. Downstream of 25, $d'<0$ and $\sigma'>0$. Therefore $B_c'=d'-h_c\sigma'/\sigma$ is positive upstream and negative downstream, for every $Q>0$. In particular,

$$x_c(Q)=25,\quad B_c''(25;Q)=-\frac{2(0.15)}{6^2}-h_c(25;Q)\frac{2(0.25)}{7^2\sigma(25)}<0. \tag{2.19}$$

The critical head is thus obtained directly from

$$B_*(Q)=0.15+\frac{3}{2}\left(\frac{Q^2}{g(0.75)^2}\right)^{1/3}.$$

For every proposed jump position $x_s\in(25,60)$, the conjugate depth satisfies $B^+>B_c(x_s;Q)$. Since B_c decreases strictly downstream, the subcritical continuation exists throughout $[x_s,60]$.

Let $H_{\mathrm{conj}}(Q)$ denote the conjugate depth at x_R of the supercritical outlet depth $H_{\mathrm{sup}}(Q)$:

$$H_{\mathrm{conj}}(Q)=\frac{H_{\mathrm{sup}}(Q)}{2}\left[\sqrt{1+\frac{8Q^2}{g\sigma(x_R)^2H_{\mathrm{sup}}(Q)^3}}-1\right]. \tag{2.20}$$

Theorem 2.3 (Controlled hydrostatic portrait). *For the geometry* (2.18) *and every* $Q>0$,

$$H_{\mathrm{sup}}(Q)<h_c(x_R;Q)<H_{\mathrm{conj}}(Q)<H_{\mathrm{sub}}(Q). \tag{2.21}$$

The shooting map is a smooth, strictly decreasing bijection

$$J_Q:(25,60)\to\left(H_{\mathrm{conj}}(Q),H_{\mathrm{sub}}(Q)\right).$$

Consequently, every downstream depth satisfying

$$H_{\mathrm{conj}}(Q)<h_R<H_{\mathrm{sub}}(Q)$$

determines exactly one controlled stationary profile with an interior entropy-admissible jump. Its position is the unique solution of $J_Q(x_s)=h_R$.

The smooth profiles are classified by (2.11). *For* $H_{\mathrm{sup}}<h_R\le H_{\mathrm{conj}}$, *there is neither a globally smooth profile nor an interior jump belonging to this controlled family.*

Proof. For $x_s>25$, both terms in the bracket in (2.16) are negative. Hence $\left(B^+\right)'<0$, and (2.17) gives $J_Q'<0$.

As $x_s\downarrow 25$, the two jump traces approach the critical depth, the jump strength vanishes, and $B^+\to B_*$. Thus

$$\lim_{x_s\downarrow 25}J_Q(x_s)=H_{\mathrm{sub}}(Q).$$

As $x_s\uparrow 60$, the jump approaches the downstream boundary, and

$$\lim_{x_s\uparrow 60}J_Q(x_s)=H_{\mathrm{conj}}(Q).$$

Conjugacy places H_{conj} on the subcritical side of $h_c(x_R;Q)$. Its head is strictly smaller than B_* by (2.14). Since the subcritical depth increases with head, $H_{\mathrm{conj}}<H_{\mathrm{sub}}$. Continuity and strict monotonicity prove the asserted bijection and uniqueness. □

The term *controlled* specifies the upstream head B_* and the subcritical-to-supercritical passage at x_c. The uniqueness statement applies to this family.

Remark 2.4 (Limiting configurations). When $h_R\downarrow H_{\mathrm{conj}}$, the controlled jump approaches x_R. When $h_R\uparrow H_{\mathrm{sub}}$, it approaches x_c with vanishing amplitude.

In the latter limit, the depth tends to the upper algebraic root on both sides of x_c, producing a corner at the control. This limiting profile differs from the smooth reverse crossing associated with the same boundary depth H_{sub} in (2.11). The interior jump family therefore corresponds to the open interval $\left(H_{\mathrm{conj}}, H_{\mathrm{sub}}\right)$.

Figure 1 represents these regimes in the $\left(Q_L, h_R\right)$ plane. The two critical curves separate the globally smooth regimes, while the conjugate curve determines the lower boundary of the controlled jump band.

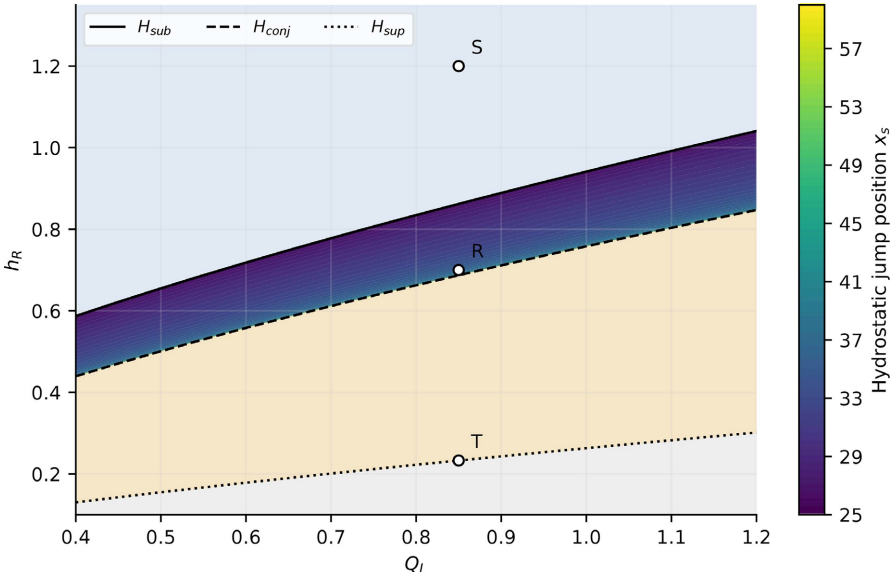


Figure 1. Hydrostatic boundary-data portrait for the Gaussian channel. The solid, dashed and dotted curves represent H_{sub}, H_{conj} and H_{sup}, respectively. The coloured band consists of controlled interior jumps, with colour indicating the jump position x_s. The region between H_{sup} and H_{conj} contains no member of this family. The points S, T and R correspond to the three reference configurations.

2.4. Construction of the Profiles and the Portrait

The construction consists of evaluating the two positive Bernoulli roots, selecting the appropriate branch on each interval, and, when necessary, locating a jump by a scalar equation.

Evaluation of the Bernoulli roots. For given x, Q and head B, define

$$E = B - d(x), \quad \lambda = \frac{E}{h_c(x;Q)}, \quad z = \frac{h}{h_c(x;Q)}.$$

The depth equation becomes

$$f_\lambda(z) := z + \frac{1}{2z^2} - \lambda = 0, \quad \text{or equivalently} \quad z^3 - \lambda z^2 + \frac{1}{2} = 0. \tag{2.22}$$

Positive roots exist if and only if $\lambda \geq 3/2$. At $\lambda = 3/2$, the critical root is $z = 1$. For $\lambda > 3/2$, the two roots can be determined separately on the explicit intervals

$$z_- \in \left(\frac{1}{\sqrt{2\lambda}}, 1\right), \quad z_+ \in (1, \lambda). \tag{2.23}$$

Indeed,

$$f_\lambda\left(\frac{1}{\sqrt{2\lambda}}\right)=\frac{1}{\sqrt{2\lambda}}>0,\quad f_\lambda(1)=\frac{3}{2}-\lambda<0,\quad f_\lambda(\lambda)=\frac{1}{2\lambda^2}>0.$$

Moreover, f_λ decreases on $(0,1)$ and increases on $(1,\infty)$. Each interval therefore contains exactly one root.

Bisection on the two intervals preserves the distinction between the supercritical and subcritical branches. If $[a_n,b_n]$ is the current bracket, the midpoint approximates the corresponding depth with error at most

$$\frac{h_c(x;Q)}{2}(b_n-a_n).$$

Thus, a prescribed absolute depth tolerance ε_h is reached when

$$\frac{h_c(x;Q)}{2}(b_n-a_n)\le\varepsilon_h.$$

The dimensional roots are then recovered as $h_-=h_c z_-$ and $h_+=h_c z_+$.

Near criticality, an equivalent residual is

$$f_\lambda(z)=\frac{(z-1)^2(2z+1)}{2z^2}-\left(\lambda-\frac{3}{2}\right). \tag{2.24}$$

This expression displays the double root at the critical state. Since $\partial_h\mathcal{B}_Q$ vanishes there, the bracket width provides a direct depth-accuracy criterion even when the head residual is very small.

Selection of a smooth profile. For prescribed (Q,h_R), first evaluate $B_*(Q)$, $H_{\sup}(Q)$, $H_{\sub}(Q)$ and $B_R(Q,h_R)$. The profile is then selected from (2.11):

$$h(x)=\begin{cases}h_-(x;B_R,Q), & 0<h_R<H_{\sup},\\ h_+(x;B_R,Q), & h_R>H_{\sub}.\end{cases}$$

On $h_R=H_{\sup}$, use (2.9); on $h_R=H_{\sub}$, use the reverse crossing. At $x=x_c$, assign $h=h_c(x_c;Q)$ directly.

The branch switch at x_c is essential for smoothness. The local expansion (2.6) also gives the limiting slope and can be used to evaluate the profile close to the control. For a transcritical reference, the boundary depth is defined by the exact relation $h_R=H_{\sup}(Q)$ or $h_R=H_{\sub}(Q)$; a displayed rounded decimal is only a numerical representation of that relation.

Location of a controlled jump. Suppose $H_{\conj}(Q)<h_R<H_{\sub}(Q)$. An equivalent form of the shooting equation is

$$G_Q(x_s):=B^+(Q,x_s)-B_R(Q,h_R)=0. \tag{2.25}$$

This formulation determines the jump position directly from the downstream head. At each trial position x_s:

1) Evaluate the supercritical root $h_s^-=h_-(x_s;B_*,Q)$.

2) Compute its conjugate depth h_s^+ from (2.13).

3) Evaluate $B^+(Q,x_s)=\mathcal{B}_Q(x_s,h_s^+)$ and hence $G_Q(x_s)$.

For the Gaussian geometry, G_Q is strictly decreasing. It extends continuously to $[x_c, x_R]$, with

$$G_Q(x_c) = B_* - B_R > 0,$$

and

$$G_Q(x_R) = \mathcal{B}_Q(x_R, H_{\text{conj}}) - B_R < 0.$$

These endpoint values provide a bracket for the unique interior root. Starting from $[a,b] = [x_c, x_R]$, evaluate G_Q at $m = (a+b)/2$. If $G_Q(m) > 0$, replace a by m; if $G_Q(m) < 0$, replace b by m. Stopping when $b - a \le 2\varepsilon_x$ determines the jump position to within ε_x, provided the signs of the evaluated residuals are resolved accurately. The Bernoulli roots used in each evaluation are refined until further refinement leaves these signs unchanged.

Once x_s is determined, the full depth is

$$h(x) = \begin{cases} h_+(x; B_*, Q), & x < x_c, \\ h_c(x_c; Q), & x = x_c, \\ h_-(x; B_*, Q), & x_c < x < x_s, \\ h_+(x; B^+(Q, x_s), Q), & x_s < x \le x_R. \end{cases} \tag{2.26}$$

At the discontinuity, retain the two traces $h(x_s^-) = h_s^-$ and $h(x_s^+) = h_s^+$ separately. In a graphical representation, both traces have the same abscissa x_s.

For any of the constructed profiles, the remaining hydraulic quantities follow from

$$A(x) = \sigma(x) h(x), \qquad u(x) = \frac{Q}{\sigma(x) h(x)},$$

$$\eta(x) = h(x) + d(x), \qquad F(x) = \frac{Q}{\sigma(x)\sqrt{g h(x)^3}}.$$

Construction of the boundary-data portrait. Choose a set of positive discharge values Q_j. For each Q_j, determine the control head $B_*(Q_j)$, evaluate the two Bernoulli roots at x_R, and compute their conjugate envelope using (2.20). The resulting curves

$$(Q_j, H_{\text{sup}}(Q_j)), \quad (Q_j, H_{\text{conj}}(Q_j)), \quad (Q_j, H_{\text{sub}}(Q_j))$$

partition the boundary-data plane.

The interior of the jump band can be parameterized directly by jump position. For each Q_j, choose $x_s \in (x_c, x_R)$, evaluate $B^+(Q_j, x_s)$, and solve the downstream subcritical Bernoulli equation to obtain $J_{Q_j}(x_s)$. Plotting

$$(Q_j, J_{Q_j}(x_s))$$

and assigning the value x_s to its colour fills the controlled jump band. Alternatively, on a prescribed (Q, h_R) grid, solve (2.25) at every point lying between H_{conj} and H_{sub}.

Verification of the constructed states. Let x_i be evaluation points away from

a jump. For a smooth profile, set $B_i = B_R$. For a controlled jump, set $B_i = B_*$ upstream of x_s and $B_i = B^+(Q, x_s)$ downstream. The principal residuals are

$$\begin{aligned} r_B &= \max_i \left| \mathcal{B}_Q\left(x_i, h(x_i)\right) - B_i \right|, \\ r_R &= \left| h(x_R) - h_R \right|, \\ r_{\mathrm{RH}} &= \left| \frac{Q^2}{\sigma_s h_s^-} + \frac{g\sigma_s \left(h_s^-\right)^2}{2} - \frac{Q^2}{\sigma_s h_s^+} - \frac{g\sigma_s \left(h_s^+\right)^2}{2} \right|, \quad \sigma_s = \sigma(x_s). \end{aligned} \tag{2.27}$$

For a jump, one additionally checks

$$F\left(x_s, h_s^-\right) > 1 > F\left(x_s, h_s^+\right), \quad B^+ < B_*,$$

together with the head-loss identity (2.14). For a smooth transcritical profile, the critical value and the one-sided slopes are checked against (2.3) and (2.6). These checks assess the Bernoulli relations, the prescribed downstream condition and the hydraulic matching conditions.

2.5. Three Reference Configurations

The comparisons with the dispersive model use the fixed discharge $Q_L = 0.85$ and three downstream depths. For this discharge, the critical and conjugate values are

$$\begin{aligned} B_* &= 0.9116814253\cdots, \\ H_{\mathrm{sup}} &= 0.2329226325\cdots, \\ H_{\mathrm{conj}} &= 0.6872527981\cdots, \\ H_{\mathrm{sub}} &= 0.8621380974\cdots. \end{aligned}$$

The three configurations are summarized in Table 1.

Table 1. Hydrostatic reference data for $Q_L = 0.85$.

Downstream depth	Regime	Construction
$h_R = 1.2$	Subcritical	$h = h_+(x; B_R, Q)$
$h_R = H_{\mathrm{sup}}(0.85)$	Smooth transcritical	(0.13)
$h_R = 0.7$	Controlled hydraulic jump	(0.30)

For the first configuration, $h_R > H_{\mathrm{sub}}$, so the profile remains subcritical throughout the channel. For the second, the subcritical and supercritical branches join smoothly at $x_c = 25$. For the third, $H_{\mathrm{conj}} < 0.7 < H_{\mathrm{sub}}$, and the unique controlled jump is located at

$$x_s = 35.99420054\cdots,$$

with traces

$$h_s^- = 0.2401915316\cdots, \quad h_s^+ = 0.6889466797\cdots.$$

The corresponding free surfaces and Froude numbers are shown in Figures 2-4.

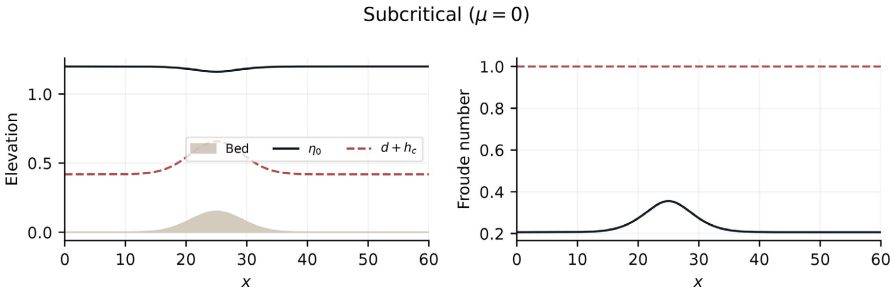


Figure 2. Hydrostatic subcritical reference: $Q_L = 0.85$ and $h_R = 1.2$. Free surface and bottom elevation (left), and Froude number (right). The depth remains above the local critical depth throughout the channel.

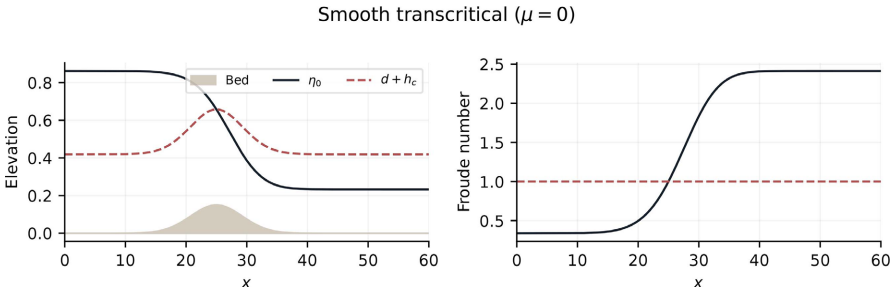


Figure 3. Hydrostatic smooth transcritical reference: $Q_L = 0.85$ and $h_R = H_{\text{sup}}(0.85) = 0.2329226325\cdots$. The subcritical upstream branch and the supercritical downstream branch meet smoothly at $x_c = 25$.

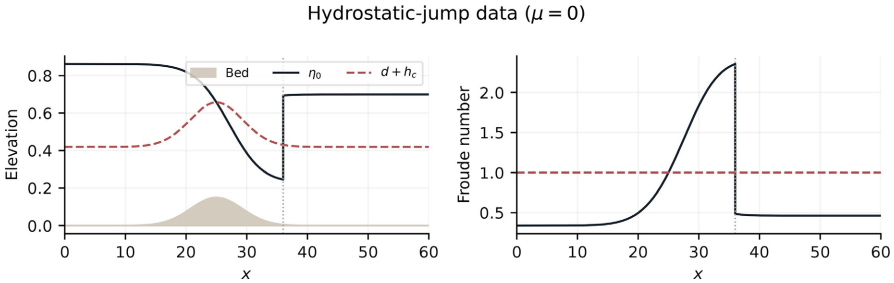


Figure 4. Hydrostatic reference with a controlled hydraulic jump: $Q_L = 0.85$ and $h_R = 0.7$. After the smooth critical passage at $x_c = 25$, the flow returns to the subcritical regime through a jump at $x_s = 35.99420054\cdots$. The jump traces satisfy the stationary momentum condition and a strictly positive hydraulic head loss.

3. Dispersive Stationary Formulation and Numerical Methods

We now consider $\mu > 0$ in (1.1), with the pressure closure (1.2)-(1.3). The hydrostatic branches constructed in Section 2 provide the reference profiles.

Two boundary formulations will be used: a continuous problem with prescribed endpoint slopes for the comparison theory, and a finite-volume problem with hydraulic data imposed through exterior states. Table 2 records their differences. The hydrostatic profiles supply reference states; sharing the numerical values of (Q_L, h_R) does not make the two dispersive boundary problems equivalent.

Table 2. Continuous and discrete dispersive boundary problems.

Feature	Continuous slope problem	Finite-volume problem
Geometry	Constant on fixed endpoint portions; localized Gaussian in Section	Original Gaussian geometry
Discharge	$Q(x) \equiv Q_L$	Constant face mass flux; Q_L is an exterior-state datum
Outlet depth	Strong trace $h(x_R) = h_R$	Exterior depth h_R entering the HLL flux
Additional closure	$h'(x_L) = h'(x_R) = 0$	Zero endpoint rows of D and prescribed pressure face fluxes
Interpretation	Conditional continuous limit theorems	Equilibria at specified mesh and continuation procedure

3.1. Continuous Boundary Problem and Stationary Pressure

We retain the interval, geometry and hydraulic variables of Section 2. For the continuous comparison results, assume $\sigma, d \in C^4(I)$, $\sigma \geq \sigma_* > 0$, and, for some fixed $0 < \rho < (x_R - x_L)/2$,

$$\sigma' = d' = 0 \quad \text{on } [x_L, x_L + \rho] \cup [x_R - \rho, x_R]. \tag{3.1}$$

Geometric variations may have finite amplitude, but are localized away from the endpoints. Section 5.1 specifies a localization of the Gaussian channel satisfying this assumption. The original Gaussian geometry remains the geometry used for the finite-volume experiments.

Stationary mass conservation gives $Q_\mu \equiv Q = Q_L > 0$. The continuous profiles satisfy

$$h_\mu'(x_L) = 0, \quad h_\mu(x_R) = h_R, \quad h_\mu'(x_R) = 0. \tag{3.2}$$

These three scalar conditions close the third-order stationary depth equation. The upstream depth and the endpoint pressures are determined as part of the solution. Throughout the continuous analysis, $h_\mu \in C^3(I)$ and $h_\mu > 0$.

Introduce the geometric coefficients

$$T(x) = \frac{Q^2}{\sigma(x)^2}, \quad \ell(x) = \frac{\sigma'(x)}{\sigma(x)}, \quad b(x) = d'(x). \tag{3.3}$$

Since $u = Q/(\sigma h_\mu)$, the quantity K in (1.3) becomes $K = -uh_\mu'/h_\mu$. Substituting this relation into the stationary pressure closure gives

$$\Pi_\mu = T\left(\frac{h_\mu''}{3} - \frac{(h_\mu')^2}{3h_\mu} + \frac{b'}{2} - \frac{bh_\mu'}{2h_\mu}\right), \tag{3.4}$$

and

$$P_{b,\mu}=\frac{3\Pi_\mu}{2h_\mu}+T\left(\frac{b'}{4h_\mu}-\frac{bh_{\mu'}}{4h_\mu^2}\right). \tag{3.5}$$

The stationary momentum equation in (1.1) then reduces to

$$g\frac{\mathrm{d}}{\mathrm{d}x}\mathcal{B}_Q\left(x,h_\mu\right)+\frac{\mu^2}{h_\mu}\left(\Pi'_\mu+bP_{b,\mu}\right)=0, \tag{3.6}$$

where $\mathcal{B}_Q$ is the hydraulic head defined in (2.2). The Froude number and critical quantities retain the definitions (2.3)-(2.5).

For the same $\left(Q,h_R\right)$ and geometry, let h_0 be the hydrostatic reference constructed in Section 2.4. Its head is B_R on a globally smooth branch and is piecewise constant on a hydraulic-jump branch. Under (3.1), every smooth hydrostatic branch is constant near the endpoints and satisfies the slope conditions in (3.2).

3.2. Stationary Balances and a Spatial First-Order System

The momentum flux and a modified hydraulic head provide useful variables for both the analysis and the continuous numerical solution. Define

$$\begin{aligned}&f\left(x,z\right)=\frac{T\left(x\right)}{z}+\frac{gz^2}{2},\quad \mathcal{C}\left(x,z\right)=gd\left(x\right)+\frac{gz}{2}-\frac{T\left(x\right)}{2z^2},\\&\mathcal{M}_\mu=f\left(x,h_\mu\right)+\mu^2\Pi_\mu.\end{aligned} \tag{3.7}$$

Here $\mathcal{M}_\mu$ is the momentum flux divided by the channel width. The contribution associated with vertical velocity is

$$\begin{aligned}&V_\mu=\frac{T}{h_\mu^2}\left(\frac{\left(h'_\mu\right)^2}{6}+\frac{bh'_\mu}{2}+\frac{b^2}{2}\right),\quad \mathcal{K}_\mu=\mu^2V_\mu,\\&\mathcal{H}_\mu=g\mathcal{B}_Q\left(x,h_\mu\right)+\mu^2\frac{\Pi_\mu}{h_\mu}+\mathcal{K}_\mu.\end{aligned} \tag{3.8}$$

Completing the square gives

$$\mathcal{K}_\mu=\frac{\mu^2T}{6h_\mu^2}\left(h'_\mu+\frac{3}{2}b\right)^2+\frac{\mu^2Tb^2}{8h_\mu^2}\geq 0, \tag{3.9}$$

while the definitions imply

$$\mathcal{H}_\mu=\mathcal{C}\left(x,h_\mu\right)+\frac{\mathcal{M}_\mu}{h_\mu}+\mathcal{K}_\mu. \tag{3.10}$$

The stationary balances are

$$\mathcal{M}'_\mu=-\ell\frac{T}{h_\mu}-gh_\mu b-\frac{3b}{2h_\mu}\left(\mathcal{M}_\mu-f\left(x,h_\mu\right)\right)-\frac{\mu^2Tbb'}{4h_\mu}+\frac{\mu^2Tb^2h'_\mu}{4h_\mu^2}, \tag{3.11}$$

and

$$\mathcal{H}'_\mu=-2\ell\mathcal{K}_\mu. \tag{3.12}$$

To obtain the first identity, differentiate (3.7) and use (3.6) to find

$$\mathcal{M}'_{\mu} = -\ell \frac{T}{h_{\mu}} - g h_{\mu} b - \mu^2 b P_{b,\mu}.$$

Substitution of (3.5) proves (3.11). Similarly,

$$\mathcal{H}'_{\mu} = \mu^2 \left(V'_{\mu} - \frac{h'_{\mu}}{h_{\mu}^2} \Pi_{\mu} - \frac{b}{h_{\mu}} P_{b,\mu} \right).$$

Using (3.4)-(3.5) and $T' = -2\ell T$ reduces the bracket to $-2\ell V_{\mu}$. Thus the modified head is constant in a channel of constant width; its variation for non-constant width is given by (3.12).

Spatial Formulation

Writing $p = h'$ and omitting the subscript μ, the preceding identities yield the equivalent system

$$\begin{aligned} h' &= p, \\ p' &= \frac{p^2}{2h} - \frac{3}{2} b' - \frac{3b^2}{2h} + \frac{3h}{\mu^2 T} \left(\mathcal{H} - g \mathcal{B}_Q (x, h) \right), \\ \mathcal{H}' &= -\frac{2\ell \mu^2 T}{h^2} \left(\frac{p^2}{6} + \frac{bp}{2} + \frac{b^2}{2} \right). \end{aligned} \tag{3.13}$$

For fixed $\mu > 0$, its right-hand side is locally Lipschitz in $(h, p, \mathcal{H})$ for $h > 0$. In particular, it remains regular at $F = 1$, because no division by $1 - F^2$ occurs. Local initial-value solutions therefore exist uniquely; solving (3.2) requires determining a positive trajectory across the entire interval.

For numerical solution, positivity is enforced by setting $z = \log h$ and $v = z' = p/h$. The transformed system is

$$\begin{aligned} z' &= v, \\ v' &= -\frac{v^2}{2} - \frac{3b'}{2\mathrm{e}^z} - \frac{3b^2}{2\mathrm{e}^{2z}} + \frac{3}{\mu^2 T} \left(\mathcal{H} - g \mathcal{B}_Q \left(x, \mathrm{e}^z \right) \right), \\ \mathcal{H}' &= -2\ell \mu^2 T \left(\frac{v^2}{6} + \frac{bv}{2\mathrm{e}^z} + \frac{b^2}{2\mathrm{e}^{2z}} \right), \end{aligned} \tag{3.14}$$

with $v(x_L) = v(x_R) = 0$ and $z(x_R) = \log h_R$. Section 5.2 describes its collocation discretization and error controls.

Local existence at fixed dispersion. The initial-value formulation also gives a local existence result for the slope boundary problem near a uniform flow. Here locality refers to the geometry and to a neighbourhood of that flow, while the dispersion is fixed.

Proposition 3.1 (Local existence near a uniform subcritical flow). *Fix* $Q > 0$, $\sigma_0 > 0$, $d_0 \in \mathbb{R}$, $\mu > 0$ *and* $H > \left(Q^2 / \left(g \sigma_0^2 \right) \right)^{1/3}$. *Set*

$$T_0 = \frac{Q^2}{\sigma_0^2}, \quad \beta = 1 - \frac{T_0}{g H^3} > 0, \quad \omega^2 = \frac{3 g H \beta}{\mu^2 T_0}, \quad L = x_R - x_L. \tag{3.15}$$

Let $s, \delta \in C^4(I)$ *vanish on fixed neighbourhoods of both endpoints, and put* $\sigma_{\varepsilon} = \sigma_0 + \varepsilon s$ *and* $d_{\varepsilon} = d_0 + \varepsilon \delta$. *If*

$$\sin(\omega L) \neq 0, \tag{3.16}$$

then, for all sufficiently small $|\varepsilon|$, *the stationary problem with this geometry and*

$$h'(x_L) = h'(x_R) = 0, \quad h(x_R) = H$$

has a positive classical solution h_ε. *It is locally unique among solutions whose initial pair* $(h(x_L), \mathcal{H}(x_L))$ *is close to* (H, E_0), *where*

$$E_0 = g\left(H + d_0 + \frac{T_0}{2gH^2}\right).$$

The corresponding spatial trajectory depends continuously differentiably on ε, *and* $h_\varepsilon \to H$ *in* $C^2(I)$ *as* $\varepsilon \to 0$.

Proof. For the perturbed geometry, solve (3.13) with initial data

$$(h, p, \mathcal{H})(x_L) = (a, 0, E).$$

At $(\varepsilon, a, E) = (0, H, E_0)$ the trajectory is the constant state $(H, 0, E_0)$. Smooth dependence for the spatial ordinary differential equation, applied on the compact interval I, gives a neighbourhood of these parameters in which trajectories exist throughout I, remain positive, and depend continuously differentiably on the parameters. Define the shooting map

$$\mathcal{S}(\varepsilon, a, E) = \left(h(x_R; \varepsilon, a, E) - H, p(x_R; \varepsilon, a, E)\right).$$

To differentiate it with respect to (a, E) at the constant state, write η for the depth variation and e for the modified-head variation. The linearized equations are

$$\eta'' + \omega^2 \eta = ce, \quad e' = 0, \quad c = \frac{3H}{\mu^2 T_0}, \quad \eta'(x_L) = 0.$$

Since $\omega^2 = cg\beta$, their solution gives

$$D_{(a,E)}\mathcal{S}(0, H, E_0) = \begin{pmatrix} \cos(\omega L) & \dfrac{1 - \cos(\omega L)}{g\beta} \\ -\omega \sin(\omega L) & \dfrac{\omega \sin(\omega L)}{g\beta} \end{pmatrix}. \tag{3.17}$$

Its determinant is $\omega \sin(\omega L)/(g\beta)$, which is nonzero by (3.16). The implicit-function theorem therefore supplies a unique nearby pair $(a(\varepsilon), E(\varepsilon))$ with $\mathcal{S} = 0$. Positivity and convergence follow from continuous dependence of the trajectory. The spatial equations give the stated depth regularity and C^2 convergence; their equivalence with the stationary pressure formulation proves that this trajectory solves the required boundary problem. □

The neighbourhood in this proposition depends on μ and on the non-resonance condition. Indeed, the resonant values

$$\mu_n = \frac{L}{n\pi}\sqrt{\frac{3gH\beta}{T_0}}, \quad n \geq 1,$$

accumulate at zero. At these values the shooting linearization is singular; the con-

stant solution still exists, and singularity alone does not establish a nonlinear bifurcation. The proposition proves existence for small geometric perturbations at fixed non-resonant dispersion. It does not provide a family for a fixed nonuniform channel as $\mu \to 0$, nor an existence result for the hydraulic-jump data. Those questions remain separate from the conditional comparison theorems in Section 4.

3.3. A Material-Derivative Pressure Variant

To examine the influence of the width-dependent pressure terms, we also consider the variant obtained by replacing the two coefficients in (1.3) by

$$\mathrm{A}_M = K^2 - (\partial_t + u\partial_x)K, \quad \mathrm{B}_M = (\partial_t + u\partial_x)(ub). \tag{3.18}$$

Denoting the main closure by W, their differences are $\mathrm{A}_M - \mathrm{A}_W = \ell u K$ and $\mathrm{B}_M - \mathrm{B}_W = -\ell u^2 b$. At constant discharge,

$$\begin{aligned} \Pi_M &= \Pi_W - T\ell\left(\frac{h'}{3} + \frac{b}{2}\right), \\ P_{b,M} &= P_{b,W} - T\ell\left(\frac{h'}{2h} + \frac{b}{h}\right). \end{aligned} \tag{3.19}$$

The two formulations agree for constant width. In a variable channel, (3.19) specifies the change in the stationary equations. The comparison theorems and the main numerical results concern W; the effect of M is examined in Section 6.4.

3.4. Finite-Volume Discretization and Boundary States

Let $\Delta x = (x_R - x_L)/N$ and $x_i = x_L + \left(i - \frac{1}{2}\right)\Delta x$, $1 \le i \le N$. The unknowns $U_i = (A_i, Q_i)$ approximate cell averages, with $\sigma_i = \sigma(x_i)$, $d_i = d(x_i)$, $h_i = A_i/\sigma_i$ and $u_i = Q_i/A_i$. The following construction uses positive depths and positive reconstructed face depths.

The centered difference operator is

$$(Df)_i = \begin{cases} 0, & i = 1 \text{ or } i = N, \\ (f_{i+1} - f_{i-1})/(2\Delta x), & 2 \le i \le N-1. \end{cases} \tag{3.20}$$

All second differences below mean the composition $D^2 = D \circ D$. In particular, this choice gives a wider interior stencil than the usual three-point second derivative. Set

$$\ell_i = \frac{(D\sigma)_i}{\sigma_i}, \quad b_i = (Dd)_i, \quad b_i' = \left(D^2 d\right)_i.$$

The endpoint rows in (3.20) are part of the discrete boundary closure. Continuous endpoint slopes are prescribed only in the separate problem (3.2).

Hydrostatic flux and geometric correction. At a face, denote the left and right cell values by subscripts L, R. Use

$$\begin{aligned}
&\sigma_* = \frac{1}{2}\left(\sigma_L + \sigma_R\right), \quad d_* = \max\left(d_L, d_R\right),\\
&h_{L,R}^* = \max\left\{0, h_{L,R} + d_{L,R} - d_*\right\},\\
&W_{L,R}^* = \left(\sigma_* h_{L,R}^*, \sigma_* h_{L,R}^* u_{L,R}\right).
\end{aligned} \tag{3.21}$$

With $F\left(A,Q;\sigma_*\right) = \left(Q, Q^2/A + gA^2/\left(2\sigma_*\right)\right)$, the HLL flux [10] is

$$\hat{F} = \begin{cases} F\left(W_L^*;\sigma_*\right), & s_L \geq 0,\\ \dfrac{s_R F\left(W_L^*;\sigma_*\right) - s_L F\left(W_R^*;\sigma_*\right) + s_L s_R\left(W_R^* - W_L^*\right)}{s_R - s_L}, & s_L < 0 < s_R,\\ F\left(W_R^*;\sigma_*\right), & s_R \leq 0, \end{cases} \tag{3.22}$$

where

$$s_L = \min\left(u_L - \sqrt{gh_L^*}, u_R - \sqrt{gh_R^*}\right), \quad s_R = \max\left(u_L + \sqrt{gh_L^*}, u_R + \sqrt{gh_R^*}\right).$$

The hydrostatic reconstruction [9] is completed by

$$c^{L,R} = \frac{g}{2}\left(\sigma_{L,R} h_{L,R}^2 - \sigma_*\left(h_{L,R}^*\right)^2\right). \tag{3.23}$$

These corrections enter the momentum balance of the two neighboring cells with their respective left and right values.

Stationary dispersive pressure. For the main closure, define

$$\begin{aligned}
C_i^0 &= -u_i\left(D^2 u\right)_i + \left(Du\right)_i^2 + u_i^2\left(\ell_i^2 - \frac{\left(D^2\sigma\right)_i}{\sigma_i}\right)\\
&\quad + \ell_i\left[D\left(u^2/2\right)\right]_i - \ell_i u_i\left(Du\right)_i,\\
B_i^0 &= u_i^2\left(\ell_i b_i + \left(D^2 d\right)_i\right) + u_i\left(Du\right)_i b_i,\\
\Pi_i^0 &= \frac{h_i^3}{3} C_i^0 + \frac{h_i^2}{2} B_i^0, \quad P_{b,i}^0 = \frac{h_i^2}{2} C_i^0 + h_i B_i^0.
\end{aligned} \tag{3.24}$$

The last two terms in C_i^0 are evaluated separately: $D\left(u^2/2\right)$ generally differs from uDu on a finite mesh. For the material variant, replace C_i^0 by $C_i^0 + \ell_i u_i\left(\left(Du\right)_i + \ell_i u_i\right)$ and B_i^0 by $B_i^0 - \ell_i u_i^2 b_i$.

The stationary residual is

$$\begin{aligned}
R_{A,i}\left(U\right) &= -\frac{\hat{F}_{A,i+1/2} - \hat{F}_{A,i-1/2}}{\Delta x},\\
R_{Q,i}\left(U\right) &= -\frac{\hat{F}_{Q,i+1/2} - \hat{F}_{Q,i-1/2}}{\Delta x} + \frac{c_{i-1/2}^R - c_{i+1/2}^L}{\Delta x}\\
&\quad + \mu^2\left[-D\left(\sigma\Pi^0\right)_i + \left(D\sigma\right)_i \Pi_i^0 - \sigma_i b_i P_{b,i}^0\right].
\end{aligned} \tag{3.25}$$

Both A_i and Q_i are unknown in $R\left(U\right) = 0$. The first equation makes the numerical mass flux constant across faces; the cell discharges are determined by the coupled nonlinear system.

Boundary fluxes. The exterior states are

$$U_{\text{ext},L} = (A_1, Q_L), \quad U_{\text{ext},R} = (\sigma_N h_R, Q_N). \tag{3.26}$$

Their geometry is copied from the adjacent cell: $(\sigma_{\text{ext},L}, d_{\text{ext},L}) = (\sigma_1, d_1)$ and $(\sigma_{\text{ext},R}, d_{\text{ext},R}) = (\sigma_N, d_N)$. Apply (3.21)-(3.22) at these boundary faces exactly as at interior faces.

The datum h_R is therefore an exterior depth entering the outlet flux. This distinction is already visible in the mass flux. At the outlet, when $s_L < 0 < s_R$, the copied geometry and identical interior and exterior discharges give

$$\hat{F}_{A,R} = Q_N + \frac{s_L s_R}{s_R - s_L} \sigma_N (h_R - h_N). \tag{3.27}$$

If both outlet wave speeds are positive, the HLL flux uses the interior state, so $\hat{F}_{A,R} = Q_N$ and the flux does not enforce $h_N = h_R$. At the inlet, the two areas agree; when $s_L < 0 < s_R$, the mass flux is

$$\hat{F}_{A,L} = \frac{s_R Q_L - s_L Q_1}{s_R - s_L}. \tag{3.28}$$

The speeds in each formula are those of the corresponding boundary face. Thus the prescribed exterior discharge Q_L need not equal the attained numerical mass flux. At stationarity it is the face flux $\hat{q}_N = \hat{F}_{A,i+1/2}$ that is constant, not necessarily the cell values Q_i or the exterior datum Q_L. The boundary discrepancy is therefore part of the specified discrete problem, rather than a residual of a strongly imposed trace.

To express the dispersive contribution as a face-flux difference, put $p_i = \sigma_i \Pi_i^0$ and set

$$\hat{p}_{i+1/2} = \frac{p_i + p_{i+1}}{2} \quad (1 \le i < N), \quad \hat{p}_{1/2} = \hat{p}_{3/2}, \quad \hat{p}_{N+1/2} = \hat{p}_{N-1/2}. \tag{3.29}$$

Then $(Dp)_i = \left(\hat{p}_{i+1/2} - \hat{p}_{i-1/2}\right) / \Delta x$ in every cell, including the endpoint cells. This identifies the pressure fluxes used at the boundaries and completes the discrete problem.

The zero endpoint rows of D are an algebraic closure, not equations requiring one-sided slopes of the computed profile to vanish. They also make the endpoint rows of D^2 zero. Consequently $\ell_i = b_i = \left(D^2 \sigma\right)_i = \left(D^2 d\right)_i = 0$ for $i = 1, N$, and (3.24) gives

$$\Pi_1^0 = \Pi_N^0 = P_{b,1}^0 = P_{b,N}^0 = 0. \tag{3.30}$$

These are endpoint cell pressures; the boundary face pressures in (3.29) can be nonzero. In the continuous slope problem, endpoint pressures are unknowns determined by the trajectory. Neither the zero rows nor the interior consistency of the stencil establish that finite-volume solutions converge to (3.2). Such a result would require a separate analysis of the effective boundary conditions and traces.

3.5. Direct Solution of the Stationary Equations

Depth positivity is enforced through the unknown vector

$$Z=\left(\zeta_1,\cdots,\zeta_N,Q_1,\cdots,Q_N\right),\quad h_i=\mathrm{e}^{\zeta_i},\quad A_i=\sigma_i\mathrm{e}^{\zeta_i}.$$

Set $\mathcal{R}(Z)=\Delta x R\left(U(Z)\right)$. A damped Newton iteration solves

$$J\left(Z^{(k)}\right)\delta Z^{(k)}=-\mathcal{R}\left(Z^{(k)}\right),\quad Z^{(k+1)}=Z^{(k)}+\alpha_k\delta Z^{(k)}. \tag{3.31}$$

The Jacobian is approximated by centered differences,

$$J_{ij}(Z)\simeq\frac{\mathcal{R}_i\left(Z+\varepsilon_j e_j\right)-\mathcal{R}_i\left(Z-\varepsilon_j e_j\right)}{2\varepsilon_j},\quad \varepsilon_j=2\times10^{-6}\max\left(1,\left|Z_j\right|\right). \tag{3.32}$$

The residual of cell i depends only on cells with indices from $i-3$ to $i+3$, truncated at the boundaries. Within each field, columns whose cell indices agree modulo seven have disjoint affected row sets. They can therefore be perturbed simultaneously, using fourteen groups for the two fields. Each column is recovered from the rows associated with its own seven-cell stencil, and the resulting sparse linear system is solved for the Newton increment.

The first trial step is

$$\alpha_k=\min\left(1,\frac{1.5}{\left\|\delta\zeta^{(k)}\right\|_\infty}\right),$$

with $\alpha_k=1$ when $\delta\zeta^{(k)}=0$. It is accepted if reconstructed face depths are positive, all quantities are finite, and

$$\left\|\mathcal{R}\left(Z^{(k)}+\alpha_k\delta Z^{(k)}\right)\right\|_2<\left(1-10^{-4}\alpha_k\right)\left\|\mathcal{R}\left(Z^{(k)}\right)\right\|_2. \tag{3.33}$$

Otherwise the step is halved, with at most 24 trial evaluations. The stopping criterion is imposed on the unscaled residual: $\left\|R(U)\right\|_\infty<2\times10^{-9}$, with at most 100 Newton iterations for each reference calculation. The extended jump refinements at $N=1280,2560$ use 8×10^{-9}.

For each of the three data in Section 2.5, initialize a 40-cell mesh with $h_i=h_0(x_i)$ and $Q_i=Q_L$. At fixed μ, continue through $N=40,80,160,320,640$. Between levels, interpolate $\log h$ and Q linearly at the new cell centers, extend their nearest endpoint values where needed, and recover $A=\sigma\exp(\log h)$. This transfers a positive initial depth to each refined mesh. The final state is also tested with the temporal operator defined next.

3.6. Temporal Pressure Inversion and Time Integration

The temporal pressure is affine in $w=u_t$. From (1.3), its discrete coefficients satisfy

$$C_i=C_i^0-(Dw)_i-\ell_i w_i,\quad B_i=B_i^0+b_i w_i.$$

Consequently,

$$\begin{aligned}
&\Pi_i=\Pi_i^0+a_i(Dw)_i+c_i w_i,\\
&P_{b,i}=P_{b,i}^0+a_{b,i}(Dw)_i+c_{b,i}w_i,\\
&a_i=-\frac{h_i^3}{3},\quad c_i=-\frac{\ell_i h_i^3}{3}+\frac{b_i h_i^2}{2},\\
&a_{b,i}=-\frac{h_i^2}{2},\quad c_{b,i}=-\frac{\ell_i h_i^2}{2}+b_i h_i.
\end{aligned} \tag{3.34}$$

Products between cell vectors below are componentwise. For a vector v, let $[v]=\operatorname{diag}(v)$. The linear dependence of the dispersive force on w is

$$L(U)=\left(-D[\sigma]+[D\sigma]\right)\left([a]D+[c]\right)-[\sigma b]\left([a_b]D+[c_b]\right). \tag{3.35}$$

Since D has only first off-diagonals, $L(U)$ has at most two off-diagonals on either side of its main diagonal.

The mass equation gives $\dot{A}=R_A(U)$, while differentiating $u=Q/A$ gives $w=\dot{Q}/A-QR_A(U)/A^2$. The momentum equation is therefore the pentadiagonal system

$$\begin{aligned} E(U)\dot{Q}&=R_Q(U)-\mu^2L(U)\left(\frac{Q}{A^2}R_A(U)\right),\\ E(U)&=I_N-\mu^2L(U)\left[A^{-1}\right]. \end{aligned} \tag{3.36}$$

Its band entries follow directly from (3.20), (3.34) and (3.35). Thus each evaluation of the temporal right-hand side consists of computing the reconstructed fluxes, evaluating $R(U)$, assembling these five diagonals, and solving (3.36) by banded elimination. Denote the resulting right-hand side by $\mathcal{F}(U)=\left(R_A(U),\dot{Q}\right)$.

If $E(U)$ is invertible, $\mathcal{F}(U)=0$ is equivalent to $R(U)=0$: the mass equation first gives $R_A=0$, after which (3.36) reduces to $E\dot{Q}=R_Q$. Both residuals are checked at accepted stationary states, together with successful solution of the temporal linear system.

Time integration uses the three-stage method [11]

$$\begin{aligned} U^{(1)}&=U^n+\Delta t_n\mathcal{F}\left(U^n\right),\\ U^{(2)}&=\frac{3}{4}U^n+\frac{1}{4}\left(U^{(1)}+\Delta t_n\mathcal{F}\left(U^{(1)}\right)\right),\\ U^{n+1}&=\frac{1}{3}U^n+\frac{2}{3}\left(U^{(2)}+\Delta t_n\mathcal{F}\left(U^{(2)}\right)\right). \end{aligned} \tag{3.37}$$

The geometry is fixed, but the pressure coefficients and temporal matrix are updated and inverted at each stage using that stage's depth. The time-step rule, acceptance criteria and stopping tests are specified in Section 7.1.

4. Hydrostatic Limit and Total Variation of Continuous Profiles

We study families of classical solutions of the continuous boundary problem in Section 3.1, using the stationary balances of Section 3.2. The geometry, discharge, downstream depth and constant endpoint portions are fixed as $\mu\to 0$. Every assertion below is conditional on the existence of the stated family. Constants may depend on these fixed data and on the assumed depth bounds, but are independent of $0<\mu\le 1$.

For a hydrostatic reference h_0, write

$$E_p(\mu)=\left\|h_\mu-h_0\right\|_{L^p(I)},\quad 1\le p\le\infty. \tag{4.1}$$

For $v \in BV(I)$, $\mathrm{TV}(v)$ denotes the mass of its distributional derivative on (x_L, x_R); for an absolutely continuous function it is $\int_I |v'| \mathrm{d}x$. Strict convergence in BV means convergence in L^1 together with convergence of total variations. Weak-* convergence in BV means L^1 convergence and weak-* convergence of the derivative measures in the open interval. Endpoint traces will be treated separately when they are needed.

4.1. Estimates at the Dispersive Scale

The flux $\mathcal{M}_\mu$, modified head $\mathcal{H}_\mu$ and nonnegative contribution $\mathcal{K}_\mu$ have already been defined in (3.7)-(3.9). Their balances provide uniform control even when derivatives of h_μ grow as the dispersive scale decreases.

Lemma 4.1 (Uniform control of rescaled dispersive variables). *Let* h_μ *solve the continuous stationary problem of Section* 3.1, *and assume*

$$0 < m \le h_\mu(x) \le M \quad (x \in I), \tag{4.2}$$

with m, M *independent of* μ. *There is a constant* C *such that*

$$\|\mathcal{M}_\mu\|_{W^{1,\infty}(I)} + \|\mathcal{H}_\mu\|_{W^{1,\infty}(I)} + \|\mu h_\mu'\|_{L^\infty(I)} + \|\mu^2 h_\mu''\|_{L^\infty(I)} + \|\mu^2 \Pi_\mu\|_{L^\infty(I)} \le C. \tag{4.3}$$

In particular,

$$\mathrm{TV}(h_\mu) \le \frac{C}{\mu}. \tag{4.4}$$

Proof. On $[x_R - \rho, x_R]$, the geometry is constant, so $\mathcal{M}_\mu$ is constant. Denote its value by J_μ, and set $z_\mu = \log h_\mu$, $T_R = T(x_R)$, and $f_R(s) = T_R/s + gs^2/2$. Equation (3.4) gives

$$z_\mu'' = \frac{3}{\mu^2 T_R h_\mu}\left(J_\mu - f_R(h_\mu)\right), \quad z_\mu'(x_R) = 0.$$

Let $f_{\min}$ and $f_{\max}$ be the extrema of f_R on $[m, M]$. If $J_\mu > f_{\max}$, then

$$z_\mu'' \ge \frac{3\left(J_\mu - f_{\max}\right)}{\mu^2 T_R M}.$$

Integrating twice from x_R and using (4.2) gives

$$\log\frac{M}{m} \ge \frac{3\left(J_\mu - f_{\max}\right)\rho^2}{2\mu^2 T_R M}.$$

Hence $J_\mu \le f_{\max} + C\mu^2$; reversing signs similarly gives $J_\mu \ge f_{\min} - C\mu^2$. Thus $|\mathcal{M}_\mu(x_R)| \le C$. Since $b(x_R) = h_\mu'(x_R) = 0$, (3.10) also gives $|\mathcal{H}_\mu(x_R)| \le C$.

From (3.9)-(3.10),

$$\mathcal{K}_\mu \le C\left(1 + |\mathcal{H}_\mu| + |\mathcal{M}_\mu|\right), \quad \mu|h_\mu'| \le C\sqrt{\mathcal{K}_\mu} + C\mu.$$

Equations (3.11)-(3.12) therefore imply

$$|\mathcal{M}_\mu'| + |\mathcal{H}_\mu'| \le C\left(1 + |\mathcal{M}_\mu| + |\mathcal{H}_\mu|\right).$$

Gronwall's inequality, applied from x_R, bounds $\mathcal{M}_\mu$ and $\mathcal{H}_\mu$ uniformly throughout I. Their derivative bounds follow from the same equations. The bound on $\mu h'_\mu$ follows from (3.9); the definition of $\mathcal{M}_\mu$ bounds $\mu^2\Pi_\mu$; and (3.4) then bounds $\mu^2 h''_\mu$. Finally,

$$\mathrm{TV}\left(h_\mu\right) \le |I| \left\| h'_\mu \right\|_{L^\infty(I)} \le C/\mu.$$

□

A useful consequence is

$$\left\| \mathcal{K}_\mu \right\|_{L^1(I)} \le C\mu \mathrm{TV}\left(h_\mu\right) + C\mu^2. \tag{4.5}$$

Indeed,

$$\mu^2 \int_I \left(h'_\mu\right)^2 \mathrm{d}x \le \left\| \mu h'_\mu \right\|_{L^\infty(I)} \mu \mathrm{TV}\left(h_\mu\right),$$

and the remaining geometric terms in V_μ satisfy the claimed bound.

4.2. Identification of Strongly Compact Limits

The following lemma supplies the mechanism common to all three regimes.

Lemma 4.2 (Every strong limit has constant hydrostatic head). *Under the assumptions of Lemma* 4.1, *suppose that, along a sequence* $\mu \to 0$, $h_\mu \to h$ *in* $L^1(I)$. *Then*

$$\mu^2 \int_I \left(h'_\mu\right)^2 \mathrm{d}x \to 0, \quad \left\| \mathcal{K}_\mu \right\|_{L^1(I)} \to 0, \quad \left\| \mu^2 \Pi_\mu \right\|_{L^1(I)} \to 0. \tag{4.6}$$

The limit has a continuous representative on I. For some constant B,

$$\mathcal{B}_Q\left(x, h(x)\right) = B \quad (x \in I). \tag{4.7}$$

It also satisfies the hydrostatic momentum balance in distributions.

Proof. For any $\varphi \in C^1(I)$, the zero slopes at both endpoints give

$$\mu^2 \int_I \left(h'_\mu\right)^2 \mathrm{d}x = -\mu^2 \int_I \left(h_\mu - \varphi\right) h''_\mu \mathrm{d}x + \mu^2 \int_I \varphi' h'_\mu \mathrm{d}x.$$

Lemma 4.1 implies

$$\mu^2 \int_I \left(h'_\mu\right)^2 \mathrm{d}x \le C \left\| h_\mu - \varphi \right\|_{L^1(I)} + C\mu \left\| \varphi' \right\|_{L^1(I)}.$$

Passing to the upper limit gives

$$\limsup_{\mu \to 0} \mu^2 \int_I \left(h'_\mu\right)^2 \mathrm{d}x \le C \left\| h - \varphi \right\|_{L^1(I)}.$$

Density of smooth functions in L^1 proves the first convergence in (4.6). The definition of V_μ then gives $\mathcal{K}_\mu \to 0$ in $L^1(I)$.

Equation (3.4) shows that $\mu^2\Pi_\mu \to 0$ in $\mathcal{D}'\left(\left(x_L, x_R\right)\right)$: integrate the h''_μ term by parts, use the preceding estimate for $\left(h'_\mu\right)^2$, and observe that the remaining terms tend to zero. The families $\mathcal{M}_\mu$ and $\mathcal{H}_\mu$ are uniformly Lipschitz. After extraction,

$$\mathcal{M}_\mu \to \mathcal{M}, \quad \mathcal{H}_\mu \to \mathcal{H} \quad \text{uniformly on } I.$$

Since $\mu^2\Pi_\mu = \mathcal{M}_\mu - f\left(x,h_\mu\right)$, its right-hand side converges strongly in L^1. Its distributional limit is zero; hence

$$\mathcal{M} = f\left(x,h\right), \quad \mu^2\Pi_\mu \to 0 \quad \text{in } L^1\left(I\right).$$

The definition of $\mathcal{H}_\mu$ yields $\mathcal{H} = g\mathcal{B}_Q\left(x,h\right)$ almost everywhere. Moreover,

$$\left\|\mathcal{H}_\mu'\right\|_{L^1(I)} \le 2\left\|\ell\right\|_{L^\infty(I)}\left\|\mathcal{K}_\mu\right\|_{L^1(I)} \to 0.$$

Thus $\mathcal{H}$ is constant, proving (4.7) almost everywhere.

To prove continuity of h, note that for each fixed x the map

$$z \mapsto \left(f\left(x,z\right), \mathcal{B}_Q\left(x,z\right)\right)$$

is injective on $\left(0,\infty\right)$. Indeed, two distinct positive depths with the same value of f are conjugate states, as in (2.12)-(2.13); their heads differ by (2.14). The limit quantities $\mathcal{M},\mathcal{H}$ are continuous, while h takes values in the compact interval $\left[m,M\right]$. Compactness and the injectivity just proved imply that their unique associated depth is continuous, including at the endpoints. This defines the continuous representative, and (4.7) holds everywhere.

Finally, passage to the limit in (3.11) gives

$$\frac{\mathrm{d}}{\mathrm{d}x} f\left(x,h\right) = -\ell\frac{T}{h} - ghb \quad \text{in } \mathcal{D}'\left(\left(x_L,x_R\right)\right), \tag{4.8}$$

the normalized hydrostatic momentum balance. Multiplication by σ recovers (2.1). □

Consequence for uniformly bounded *BV* families. If, in addition to (4.2),

$$\sup_\mu \mathrm{TV}\left(h_\mu\right) < \infty,$$

then BV compactness gives an L^1-convergent subsequence. Every such limit is a continuous hydrostatic profile with constant head. However, L^1 convergence alone does not preserve the downstream boundary value: a boundary layer may alter the trace of the limit. The regime assumptions below resolve this issue without prescribing an additional pressure condition.

4.3. The Smooth Subcritical Branch

Theorem 4.3 (Convergence of a uniformly subcritical family). *Suppose that* $\left(Q,h_R\right)$ *defines a smooth, uniformly subcritical hydrostatic branch* h_0. *Let* h_μ *solve* (3.2) *and* (3.4)-(3.6), *with* (4.2) *and* $\sup_\mu \mathrm{TV}\left(h_\mu\right) < \infty$. *Assume that for some* $\theta \in \left(0,1\right)$,

$$F^2\left(x,h_\mu\left(x\right)\right) \le 1-\theta \quad \left(x \in I\right). \tag{4.9}$$

Then

$$h_\mu \to h_0 \ \text{ uniformly on } \ I, \ \ h_\mu \rightharpoonup^* h_0 \ \text{ in } \ BV\left(I\right), \tag{4.10}$$

and

$$\mathrm{TV}\left(h_0\right) \le \liminf_{\mu\to 0} \mathrm{TV}\left(h_\mu\right).$$

If each h_μ *has a partition into at most* N *intervals of monotonicity, with* N *independent of* μ, *then*

$$\mathrm{TV}(h_\mu) \to \mathrm{TV}(h_0), \tag{4.11}$$

so the convergence is strict in BV.

Proof. Compactness in BV and Lemma 4.2 give, after extraction, $h_\mu \to h$ in L^1, with

$$\mathcal{M} = f(x,h), \quad \mathcal{H} = g\mathcal{B}_Q(x,h) \quad \text{constant.}$$

The limit remains uniformly subcritical. Set

$$\Psi(x,z;J) = \mathcal{C}(x,z) + \frac{J}{z}.$$

Then

$$\partial_z \Psi(x,z;J) = \frac{f(x,z) - J}{z^2}.$$

For $J = f(x,h(x))$, the uniform subcritical gap and the depth bounds imply, for z between $h_\mu(x)$ and $h(x)$,

$$\Psi(x,z;J) - \Psi(x,h(x);J) \geq c\left|z - h(x)\right|^2$$

with $c > 0$ independent of x, μ. This follows by integrating the preceding derivative and using $\partial_z f = gz\left(1 - F^2(x,z)\right) \geq gm\theta$ on this interval of depths. By (3.10) and $\mathcal{K}_\mu \geq 0$,

$$\Psi(x,h_\mu;\mathcal{M}_\mu) \leq \mathcal{H}_\mu.$$

Uniform convergence of $\mathcal{M}_\mu, \mathcal{H}_\mu$ therefore gives $\|h_\mu - h\|_{L^\infty(I)} \to 0$. In particular, $h(x_R) = h_R$, so its head is $B_R(Q,h_R)$. Uniqueness of the subcritical root implies $h = h_0$. Every extracted limit is the same; hence the whole family converges. The weak-* BV statement and lower semicontinuity follow.

For the last assertion, choose monotonicity partitions with at most N intervals. After extraction, the partition points converge. Uniform convergence implies that the sum of the endpoint differences on these partitions converges to a sum of differences of values of h_0, which is at most $\mathrm{TV}(h_0)$. Thus

$$\limsup_{\mu \to 0} \mathrm{TV}(h_\mu) \leq \mathrm{TV}(h_0).$$

Lower semicontinuity supplies the reverse inequality. □

A uniform bound on the number of monotonicity intervals already implies a BV bound, since $\mathrm{TV}(h_\mu) \leq N(M-m)$.

Corollary 4.4 (A rate on uniformly regular subcritical families). *Assume that* h_0 *and an existing family* h_μ *solve the corresponding hydrostatic and dispersive stationary problems with the same trace* h_R, *satisfy* $m \leq h_0, h_\mu \leq M$ *and* $F^2(x,h_0), F^2(x,h_\mu) \leq 1-\theta$, *and that* $\sup_\mu \|h_\mu\|_{W^{3,\infty}(I)} < \infty$. *Then*

$$\|h_\mu - h_0\|_{W^{1,\infty}(I)} \leq C\mu^2, \quad \left|\mathrm{TV}(h_\mu) - \mathrm{TV}(h_0)\right| \leq C\mu^2.$$

In particular $E_p(\mu) \le C_p \mu^2$ *for* $1 \le p \le \infty$. *This rate requires substantially more than the rescaled derivative bounds of Lemma* 4.1.

Proof. The closure and the uniform $W^{3,\infty}$ bound give $\left\| h_\mu^{-1} \left(\Pi'_\mu + bP_{b,\mu} \right) \right\|_\infty \le C$. Integrating (3.6) from x_R gives $\left\| \mathcal{B}_Q(x, h_\mu) - B_R \right\|_\infty \le C\mu^2$. On the interval of depths between $h_\mu(x)$ and $h_0(x)$, $\partial_h \mathcal{B}_Q = 1 - F^2 \ge \theta$, because both endpoints are uniformly subcritical. The mean-value theorem yields the depth estimate. Next write

$$\left(1 - F^2\left(x, h_\mu\right)\right) h'_\mu = -b + \frac{\ell T}{g h_\mu^2} - \frac{\mu^2}{g h_\mu} \left(\Pi'_\mu + bP_{b,\mu} \right).$$

Subtract the hydrostatic identity, use the depth estimate, smooth dependence on $h \in [m, M]$ and the subcritical gap, and divide by $1 - F^2$. This proves the derivative estimate. Finally, $\left| \mathrm{TV}\left(h_\mu\right) - \mathrm{TV}\left(h_0\right) \right| \le \int_I \left| h'_\mu - h'_0 \right| \mathrm{d}x$. □

4.4. The Smooth Transcritical Branch

Assume now that $B_c(\cdot; Q)$ has a unique interior nondegenerate maximum x_c, and that

$$B_R(Q, h_R) = B_*(Q) = \max_{x \in I} B_c(x; Q), \quad h_R < h_c(x_R; Q). \tag{4.12}$$

The reference h_0 is subcritical to the left of x_c and supercritical to its right. The regularity required for smooth matching at x_c is local: for instance, one may assume that σ, d are analytic near x_c and use the argument of Proposition 2.1 there. Global analyticity is not imposed, since it would be incompatible with nonconstant geometry having exactly constant endpoint portions.

Theorem 4.5 (Convergence of a smooth transcritical family). *Under* (4.12) *and the preceding assumptions on the control point, let* h_μ *solve* (3.2) *and* (3.4)-(3.6), *with* (4.2) *and* $\sup_\mu \mathrm{TV}\left(h_\mu\right) < \infty$. *Assume there are fixed endpoint neighbourhoods and* $\theta > 0$ *on which*

$$F^2\left(x, h_\mu(x)\right) \le 1 - \theta \ \text{ near } x_L, \quad F^2\left(x, h_\mu(x)\right) \ge 1 + \theta \ \text{ near } x_R. \tag{4.13}$$

Then

$$h_\mu \to h_0 \ \text{ in } L^1(I), \quad h_\mu \overset{*}{\rightharpoonup} h_0 \ \text{ in } BV(I). \tag{4.14}$$

The convergence also holds in $L^p(I)$ *for every* $1 \le p < \infty$. *If the profiles* h_μ *are nonincreasing on all of* I, *then*

$$h_\mu \to h_0 \ \text{ uniformly on } I, \quad \mathrm{TV}\left(h_\mu\right) \to \mathrm{TV}\left(h_0\right). \tag{4.15}$$

Proof. By *BV* compactness and Lemma 4.2, every sequence has an L^1-convergent subsequence with a continuous limit h of constant head. To identify this head using the downstream datum, restrict to a fixed downstream interval where the geometry is constant and the family is uniformly supercritical. Set

$$p_\mu = \mu^2 \Pi_\mu(x_R) = \mathcal{M}_\mu(x_R) - f_R\left(h_R\right).$$

The function f_R is strictly decreasing in the supercritical region. With

$z_\mu(t) = \log h_\mu(x_R - t)$, we have

$$z'_\mu(0) = 0, \quad z''_\mu(t) = \frac{3}{\mu^2 T_R h_\mu(x_R - t)}\Big[p_\mu + f_R(h_R) - f_R\big(h_\mu(x_R - t)\big)\Big].$$

If $p_\mu > 0$, the depth initially increases as t increases. While it remains supercritical, monotonicity of f_R reinforces this sign, giving

$$z''_\mu(t) \geq \frac{3p_\mu}{\mu^2 T_R M}.$$

The depth bounds and the fixed length of the downstream interval imply $p_\mu \leq C\mu^2$. Reversing signs handles $p_\mu < 0$; therefore $|p_\mu| \leq C\mu^2$. At the right endpoint $h'_\mu = b = 0$, so

$$\mathcal{H}_\mu(x_R) = gB_R(Q, h_R) + \frac{p_\mu}{h_R} \to gB_R(Q, h_R).$$

Consequently $\mathcal{B}_Q\big(x, h(x)\big) = B_R(Q, h_R) = B_*(Q)$. The subcritical upstream regime and supercritical downstream regime select the two roots. Since h is continuous and those roots meet only at x_c, the limit is exactly h_0. Uniqueness of this limit proves convergence of the whole family. The uniform depth bounds upgrade L^1 convergence to convergence in every finite L^p.

The subcritical convexity argument in the proof of Theorem 4.3, applied near x_L, also yields $h_\mu(x_L) \to h_0(x_L)$. If the profiles are nonincreasing, L^1 convergence to continuous h_0, together with convergence of the endpoint values, implies uniform convergence. Moreover,

$$\mathrm{TV}(h_\mu) = h_\mu(x_L) - h_R \to h_0(x_L) - h_R = \mathrm{TV}(h_0).$$

□

The regime assumptions select a family of profiles; they are not additional boundary conditions.

4.5. Variation Defects and Small-Amplitude Oscillations

Even when the hydrostatic limit is smooth, convergence of depths does not necessarily imply convergence of total variations. For the families in Theorems 4.3 and 4.5, both endpoint values converge to those of h_0. After extraction, regard the following as finite Radon measures on the compact interval I:

$$|h'_\mu|\,\mathrm{d}x \rightharpoonup^* \lambda, \quad h'_\mu \mathrm{d}x \rightharpoonup^* h'_0 \mathrm{d}x.$$

For the signed measures, this follows by integration by parts using L^1 convergence and the endpoint limits. Lower semicontinuity of variation then yields

$$\lambda = |h'_0|\,\mathrm{d}x + \nu, \quad \nu \geq 0. \tag{4.16}$$

The measure ν, which may also charge the endpoints, is the variation defect. Since the measures are considered on I,

$$\lim_{\mu \to 0} \mathrm{TV}(h_\mu) = \mathrm{TV}(h_0) + \nu(I) \tag{4.17}$$

along the extracted subsequence. Strict convergence corresponds to the absence of this defect.

Proposition 4.6 (Uniform convergence can leave a variation defect). *In a constant-width channel with a flat bed, there are exact stationary solutions satisfying*

$$h_{\mu'}(x_L) = h'_{\mu}(x_R) = 0, \quad h_{\mu}(x_R) = H,$$

which converge uniformly to the constant subcritical profile $h_0 = H$ *along a sequence* $\mu \to 0$, *but whose total variations do not tend to zero.*

Proof. Set $T = Q^2/\sigma^2$ and choose $H > (T/g)^{1/3}$. For $a < H$ sufficiently close to H, define $r_a = T/(gaH) < a$. The constant-geometry first integrals give smooth periodic profiles oscillating between a and H, characterized by

$$(h'_{\mu})^2 = \frac{3g}{\mu^2 T}(H - h_{\mu})(h_{\mu} - a)(h_{\mu} - r_a). \tag{4.18}$$

Their constant flux and head are

$$\mathcal{M} = \frac{gaH}{2} + \frac{T(a+H)}{2aH}, \quad \mathcal{H} = gd + \frac{g(a+H)}{2} + \frac{T}{2aH}.$$

Substitution in (3.10) verifies (4.18). Equivalently, the profile solves the smooth second-order equation obtained by differentiating (4.18); this continues it smoothly through its turning points. Equation (3.4) then gives $\mu^2 \Pi_{\mu} = \mathcal{M} - f(h_{\mu})$, so it is an exact stationary solution of the closure.

In the coordinate x/μ, its period is

$$P(a) = 2\sqrt{\frac{T}{3g}} \int_a^H \frac{\mathrm{d}z}{\sqrt{(H-z)(z-a)(z-r_a)}}.$$

As $a \uparrow H$, this tends to a strictly positive constant (the change of variable $z = a + (H-a)s$ removes the endpoint singularities). Choose

$$a_n = H - \frac{\alpha}{n}, \quad \mu_n = \frac{|I|}{nP(a_n)},$$

with $\alpha > 0$ fixed and n sufficiently large, and put a maximum at x_R. There are exactly n periods on I, so both boundary slopes vanish. We have

$$\left\| h_{\mu_n} - H \right\|_{L^{\infty}(I)} = \frac{\alpha}{n} \to 0,$$

whereas

$$\mathrm{TV}(h_{\mu_n}) = 2n(H - a_n) = 2\alpha. \tag{4.19}$$

Thus convergence is uniform but not strict in BV. □

This example separates convergence of depths from disappearance of oscillations at the level of total variation. It also explains why stronger conclusions require a hypothesis preventing an increasing number of oscillations.

4.6. The Branch Containing a Hydraulic Jump

Let h_0 be the controlled hydrostatic profile of Section 2.2, with a nonzero jump

at x_s. The conjugate traces satisfy $h_s^- < h_s^+$, and (2.14) gives the strict head loss $B^- > B^+$, where $B^- = B_*(Q)$ and $B^+ = B_R(Q, h_R)$.

Theorem 4.7 (Obstruction to a strong hydraulic-jump limit). *Let h_μ be a family of stationary dispersive solutions satisfying* (3.1), (3.2), (3.4)-(3.6), *and the uniform depth bounds* (4.2). *No uniform total-variation bound is assumed. Then*

$$\liminf_{\mu\to 0} \|h_\mu - h_0\|_{L^1(I)} > 0. \tag{4.20}$$

In particular, the family cannot converge to h_0 strongly in L^1, weakly- in BV, or strictly in BV.*

Proof. If the lower limit in (4.20) were zero, there would be a sequence $\mu_n \to 0$ with $h_{\mu_n} \to h_0$ in $L^1(I)$. Lemma 4.2 would then force $\mathcal{B}_Q(x, h_0(x))$ to be constant. But this function equals B^- and B^+ on the two sides of the jump, with $B^- \neq B^+$ by (2.14). This is a contradiction. □

Within the uniformly positive and bounded depth class, the dissipative hydrostatic jump is therefore not a strong limit of stationary profiles of the inviscid dispersive closure. This obstruction holds even without a uniform BV bound.

Corollary 4.8 (Loss of the BV bound with a subcritical outlet). *Suppose that the downstream data belong to the controlled-jump band, so that*

$$B_R(Q, h_R) < B_*(Q) = \max_{x\in I} B_c(x; Q). \tag{4.21}$$

Let h_μ satisfy the stationary problem and uniform depth bounds of Theorem 4.7. *Assume that the family is uniformly subcritical on a fixed neighbourhood of x_R, namely $F^2(x, h_\mu(x)) \le 1-\theta$ there for some $\theta > 0$. Then*

$$\mathrm{TV}(h_\mu) \to +\infty. \tag{4.22}$$

The upper bound $\mathrm{TV}(h_\mu) \le C/\mu$ remains valid.

Proof. If the total variations did not tend to infinity, a subsequence would be bounded in BV. It would have a strong L^1 limit h, continuous and of constant head by Lemma 4.3. The subcritical convexity argument of Theorem 4.3, applied near the outlet, preserves the trace h_R. Hence $\mathcal{B}_Q(x, h(x)) = B_R(Q, h_R)$. At a point maximizing $B_c(\cdot; Q)$ this equation has no positive root because of (4.21), a contradiction. □

Without a downstream regime assumption, BV compactness alone does not exclude loss of the downstream trace in a boundary layer and convergence to a different continuous hydrostatic profile. Such a limit would not be convergence to the hydraulic-jump reference h_0.

Finally, if an oscillatory family contains N_μ disjoint complete oscillations, each with a crest-to-trough amplitude at least $a_* > 0$, then

$$\mathrm{TV}(h_\mu) \ge 2a_* N_\mu.$$

Thus $N_\mu \ge c/\mu$ implies $\mathrm{TV}(h_\mu) \ge 2a_* c/\mu$. This is the variation cost of a persistent wave train; it does not assert that every solution of the boundary problem selects such a train.

4.7. Subsequential Oscillatory Limits and Averaged Balances

The obstruction to strong convergence leaves open oscillatory limits. The same a priori estimates give necessary averaged balances for such limits, without a uniform total-variation bound. We use Y_x for a Young measure, to distinguish it from the variation defect measure ν in (4.16), and write $\langle \mathrm{Y}_x, \Phi \rangle = \int \Phi(z)\,\mathrm{dY}_x(z)$.

Proposition 4.9 (Averaged balances for bounded stationary families). *Let* $\mu_j \to 0$, *and suppose that* h_{μ_j} *satisfies the assumptions of Lemma* 4.1 *with fixed data and* $0 < m \le h_{\mu_j} \le M$. *After extraction, there are probability measures* Y_x *supported on* $[m, M]$, *functions* $\mathcal{M}, \mathcal{H} \in W^{1,\infty}(I)$ *and* $k \in L^\infty(I)$, $k \ge 0$, *such that*

$$\begin{aligned} &\Phi(h_{\mu_j}) \rightharpoonup^* \langle \mathrm{Y}_x, \Phi \rangle && \text{in } L^\infty(I), \quad \Phi \in C([m,M]), \\ &\mathcal{M}_{\mu_j} \to \mathcal{M}, \mathcal{H}_{\mu_j} \to \mathcal{H} && \text{uniformly on } I, \\ &\mathcal{K}_{\mu_j} \rightharpoonup^* k && \text{in } L^\infty(I). \end{aligned} \tag{4.23}$$

With T, ℓ, b *as in* (3.3), *the limits satisfy, almost everywhere for the algebraic identities and in distributions for the differential identities*,

$$\begin{aligned} &\mathcal{H} = g\langle \mathrm{Y}_x, \mathcal{B}_Q(x,\cdot)\rangle + k, \quad \mathcal{H}' = -2\ell k, \\ &\mathcal{M}' = -\ell T\langle \mathrm{Y}_x, z^{-1}\rangle - gb\langle \mathrm{Y}_x, z\rangle, \\ &\mathcal{M}\langle \mathrm{Y}_x, z^{-1}\rangle = T\langle \mathrm{Y}_x, z^{-2}\rangle + \frac{g}{2}\langle \mathrm{Y}_x, z\rangle. \end{aligned} \tag{4.24}$$

Here z *denotes the depth variable in the integrals. If* $h_{\mu_j} \to h$ *strongly in* $L^1(I)$, *then* $\mathrm{Y}_x = \delta_{h(x)}$ *almost everywhere and* $k = 0$.

Proof. The compact-range case of the fundamental theorem for Young measures [12] gives the first convergence in (4.23). Lemma 4.1 and (3.10) bound the other quantities in the spaces stated above. Arzelà-Ascoli and weak-* compactness, followed by a common subsequence, give their limits. Nonnegativity of $\mathcal{K}_{\mu_j}$ gives $k \ge 0$.

The weighted pressure has the exact representation

$$\frac{\Pi_\mu}{h_\mu} = \frac{T}{3}\left(\log h_\mu\right)'' + \frac{Tb'}{2h_\mu} + \frac{Tb}{2}\left(h_\mu^{-1}\right)'. \tag{4.25}$$

For a compactly supported smooth test function, integrate the first term twice and the last term once by parts. Uniform boundedness of $\log h_\mu$ and h_μ^{-1}, together with the fixed smooth coefficients, proves

$$\mu^2 \frac{\Pi_\mu}{h_\mu} \to 0 \quad \text{in } \mathcal{D}'((x_L, x_R)).$$

This family is uniformly bounded in $L^\infty(I)$ by Lemma 4.1; density of test functions in $L^1(I)$ upgrades the convergence to weak-* convergence in $L^\infty(I)$.

Passing to the limit in the definition of $\mathcal{H}_\mu$ and in (3.12) gives the first line of

(4.24). In (3.11), the pressure term is $-3b\mu^2\Pi_\mu/(2h_\mu)$ and tends weakly to zero. The term containing bb' is $O(\mu^2)$ uniformly, and the last term is $O(\mu)$ because $\mu h'_\mu$ is uniformly bounded. This gives the stated balance for $\mathcal{M}'$. Finally, divide $\mathcal{M}_\mu = f(x,h_\mu)+\mu^2\Pi_\mu$ by h_μ. Uniform convergence of $\mathcal{M}_\mu$, the weighted-pressure limit and Young-measure convergence yield the last identity. Strong L^1 convergence and the compact depth range give the Dirac measure assertion. Lemma 4.2 then gives $\mathcal{K}_{\mu_j}\to 0$ in L^1, hence $k=0$. □

These identities describe necessary constraints on subsequential oscillatory limits of existing families. They do not close an evolution or modulation system for Y_x, establish existence of a hydraulic-jump-data family, or select a unique averaged profile. In particular, the mean depth $\overline{h}(x)=\langle \mathrm{Y}_x, z\rangle$ cannot in general be substituted for the measure in the nonlinear hydraulic head. Nor does this compactness argument preserve a boundary trace of $\overline{h}$. Section 5.4 gives an exact constant-geometry example for which the measure is explicit.

4.8. Conclusions of the Comparison

For a uniformly subcritical family, a uniform total-variation bound identifies the limit and yields uniform convergence to h_0. Convergence of total variations additionally requires absence of a variation defect; a uniform bound on the number of monotonicity intervals is sufficient.

For the smooth transcritical branch, the upstream and downstream regimes select the hydrostatic matching. Strong L^1 and weak-* BV convergence hold despite the degeneracy of $1-F^2$ at the control. A nonincreasing family converges uniformly and strictly in BV.

For the hydraulic-jump branch, hydrostatic head loss is incompatible with a strong limit of uniformly positive and bounded stationary dispersive depths. If a fixed outlet neighbourhood remains subcritical, total variations necessarily diverge.

The slope conditions supply the additional stationary boundary data, but do not suppress oscillatory mechanisms as $\mu\to 0$.

Proposition 3.1 supplies local existence near uniform flow at fixed non-resonant dispersion. Existence and selection of families for a fixed nonuniform geometry as $\mu\to 0$, and their uniform depth bounds, remain separate questions. Proposition 4.9 describes necessary averaged balances for bounded families that may fail strong compactness; it does not select their oscillatory limit.

5. Continuous Numerical Illustrations of the Comparison Results

We first approximate the continuous slope problem of Section 3.1. The computations use the spatial system (3.14) and are compared with hydrostatic references for exactly the same geometry. Exact periodic solutions then illustrate separately the variation defect and the μ^{-1} variation scale established in Section 4.

5.1. Localized Geometry and Hydrostatic References

To impose (3.1), introduce the cutoff

$$S(t)=\begin{cases}0, & t\le 0,\\ 126t^5-420t^6+540t^7-315t^8+70t^9, & 0<t<1,\\ 1, & t\ge 1,\end{cases} \tag{0.94}$$

$$\chi(x)=S\left(\frac{x-2}{3}\right)S\left(\frac{58-x}{3}\right).$$

Multiply the two Gaussian amplitudes in (2.18) by χ, keeping the base width equal to one. The resulting σ,d belong to $C^4(I)$, are exactly constant on $[0,2]\cup[58,60]$, and coincide with the Gaussian geometry on $[5,55]$. They remain analytic near the control point $x_c=25$. Geometric derivatives in (3.14) are obtained by differentiating these expressions, including the cutoff factors.

The three reference profiles are constructed by the procedure of Section 2.4, now evaluated with the localized geometry. The discharge is $Q=0.85$, with $g=9.81$. The subcritical and jump data retain $h_R=1.2$ and $h_R=0.7$, respectively. For the smooth transcritical case, the outlet depth is recomputed from (4.12); the change in endpoint geometry makes it slightly different from the Gaussian value of Section 2.5.

5.2. Collocation, Continuation and Residual Control

Write (3.14) as $y'=G_\mu(x,y)$, with $y=(z,v,\mathcal{H})$. We use a fourth-order collocation method with a continuously differentiable piecewise cubic interpolant [13]. Let x_j,x_{j+1} be consecutive nodes, $\delta_j=x_{j+1}-x_j$, $x_{j+1/2}=\left(x_j+x_{j+1}\right)/2$, and $G_j=G_\mu(x_j,y_j)$. Cubic Hermite interpolation gives

$$\begin{aligned} y_{j+1/2}&=\frac{y_j+y_{j+1}}{2}-\frac{\delta_j}{8}\left(G_{j+1}-G_j\right),\\ 0&=y_{j+1}-y_j-\frac{\delta_j}{6}\left(G_j+4G_\mu\left(x_{j+1/2},y_{j+1/2}\right)+G_{j+1}\right).\end{aligned} \tag{5.2}$$

These equations are solved simultaneously with the three boundary conditions following (3.14). The nonlinear iteration uses damped Newton steps, with a line search based on the squared norm of the Newton correction. Derivatives of G_μ are approximated by forward differences with perturbations $\sqrt{\varepsilon_{\text{mach}}}\left(1+\left|y_{j,k}\right|\right)$ in component k. Sparse factorization accounts for the coupling of adjacent nodes and the endpoint conditions.

For the interpolant y_h, define the differential residual $r=y_h'-G_\mu(x,y_h)$ and the interval indicator

$$\rho_j^2=\frac{1}{\delta_j}\int_{x_j}^{x_{j+1}}\sum_{k=1}^{3}\left|\frac{r_k(x)}{1+\left|G_{\mu,k}\left(x,y_h(x)\right)\right|}\right|^2\mathrm{d}x. \tag{5.3}$$

The integral is estimated by five-point Lobatto quadrature. The endpoint residuals vanish for the Hermite interpolant; the remaining quadrature points are the

midpoint and $x_{j+1/2} \pm \frac{1}{2}\delta_j\sqrt{3/7}$. Intervals with $\tau < \rho_j < 100\tau$ are bisected, and those with $\rho_j \geq 100\tau$ are divided into three equal parts. The interpolant supplies the initial values on the refined mesh. A solution is accepted when every $\rho_j \leq \tau$ and each boundary residual has absolute value below $\tau/10$.

The first calculation starts from 2401 equally spaced nodes and the hydrostatic initial values

$$z_j = \log h_0(x_j), \quad v_j \simeq (\log h_0)'(x_j), \quad \mathcal{H}_j = gB_R.$$

The initial derivative is obtained by centered differences in the interior and one-sided differences at the endpoints. For each smooth reference, continuation proceeds through $\mu = 1, 1/2, 1/4, 1/8, 1/16$. At every new value of μ, the previous accepted cubic interpolant is evaluated on a fresh 2401-node grid. The first residual tolerance is $\tau = 10^{-8}$, with at most 120,000 nodes. An accepted solution is used to initialize a second calculation on the same starting grid, with $\tau = 10^{-10}$ and at most 240,000 nodes. The tighter solution is retained when it satisfies the stopping tests; otherwise the first solution is kept and identified as having passed only the initial tolerance.

For the norms (4.1), evaluate the retained interpolant and its hydrostatic reference at 120,001 equally spaced points. Composite Simpson quadrature gives E_1, E_2^2 and $\mathrm{TV}(h_\mu) = \int_I \left| \mathrm{e}^z v \right| \mathrm{d}x$; the largest sampled depth difference gives E_∞. The maximum depth difference between the two accepted tolerance levels measures sensitivity to the collocation tolerance. It is a numerical accuracy diagnostic, separate from the hypotheses of the comparison theorems.

5.3. Smooth Profiles and Hydraulic-Jump Data

For the subcritical data, all five dispersion values satisfy both tolerance levels, with a maximum depth difference below 8×10^{-12}. Table 3 gives the errors relative to the localized hydrostatic reference.

Table 3. Continuous subcritical profiles: depth errors and total variation for the localized Gaussian channel.

μ	E_1	E_2	E_∞	$TV(h_\mu)$
1	7.46×10^{-4}	1.72×10^{-4}	6.27×10^{-5}	0.37670393
0.5	1.86×10^{-4}	4.28×10^{-5}	1.55×10^{-5}	0.37677663
0.25	4.64×10^{-5}	1.07×10^{-5}	3.86×10^{-6}	0.37679517
0.125	1.16×10^{-5}	2.67×10^{-6}	9.65×10^{-7}	0.37679983
0.0625	2.90×10^{-6}	6.68×10^{-7}	2.41×10^{-7}	0.37680099

The observed orders $\log_2\left(E_\infty(\mu)/E_\infty(\mu/2)\right)$ are approximately 2.02, 2.00, 2.00 and 2.00. They agree with the quadratic estimate of Corollary 4.4 over the tested range. That corollary also requires uniform regularity as $\mu \to 0$, which a

finite collection of profiles cannot establish.

For the transcritical data, the solutions at $\mu = 1, 1/2, 1/4$ pass both tolerance levels and differ by less than 3×10^{-9} in depth. Their respective maximum errors are approximately 1.75×10^{-2}, 5.14×10^{-3} and 2.01×10^{-3}. Figure 5 collects the error and variation diagnostics. Figure 6 shows upstream oscillations, so the monotonicity hypothesis used for strict BV convergence in Theorem 4.5 does not apply to these computed profiles. At $\mu = 1/8$, the first tolerance is attained but the tighter calculation exhausts its node budget. At $\mu = 1/16$, the first tolerance is not attained. The $\mu = 1/8$ point in Figure 5 therefore represents the first tolerance only. These results resolve several positive-dispersion profiles without determining a transcritical asymptotic error rate.

For the jump data, each of $\mu = 1, 1/2, 1/4$ is attempted independently from the hydrostatic profile, with tolerance 10^{-7} and at most 50,000 nodes. Table 4 records the outcomes of these attempts. No calculation satisfies the acceptance tests.

Table 4. Reported collocation attempts for hydraulic-jump data. Each attempt starts independently from the hydrostatic reference.

μ	Numerical outcome	Mathematical status
1	Node budget exhausted	Existence unresolved
1/2	Singular Newton Jacobian	Existence unresolved
1/4	Singular Newton Jacobian	Existence unresolved

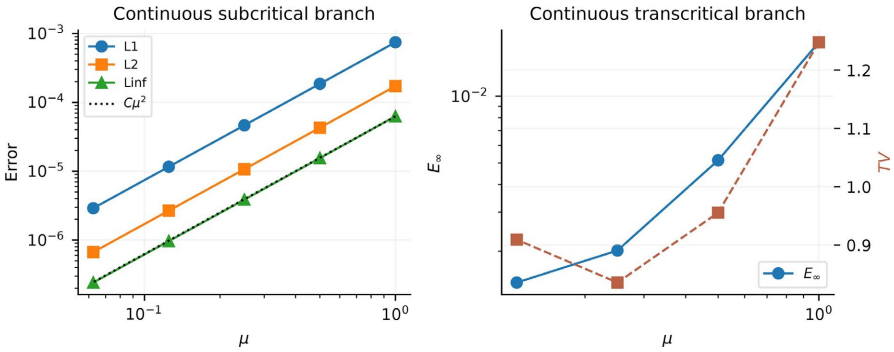


Figure 5. Continuous collocation for the localized geometry and boundary conditions (0.33). The subcritical depth errors follow a quadratic trend. The transcritical errors and total variations have a different dependence on μ; the $\mu = 1/8$ point satisfies only the 10^{-8} residual tolerance.

These outcomes characterize the stated attempts, not the solution set of the continuous boundary problem. In particular, a singular discrete Newton Jacobian does not distinguish a continuous bifurcation from poor conditioning, insufficient resolution or an unsuitable initial guess. The local existence result of Proposition 3.1 concerns a different neighbourhood and does not settle these jump-data cases. A continuation in geometry amplitude or by pseudo-arclength, with residual and conditioning diagnostics, would be needed to investigate the unresolved

branches further. Such a continuation is not part of the reported computations.

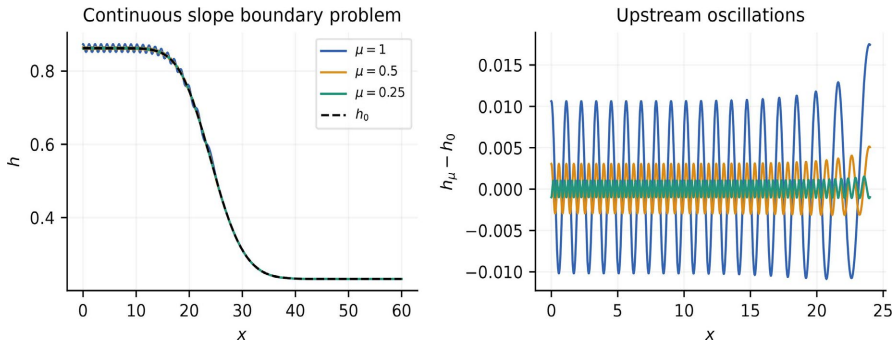


Figure 6. Transcritical profiles of the continuous slope problem at $\mu = 1, 1/2, 1/4$. The right panel magnifies the upstream oscillations.

Theorem 4.7 remains a conditional obstruction to strong convergence of bounded existing families; it is not a nonexistence theorem at any tested value of μ. The finite-volume profiles in Section 6 satisfy the different boundary closure (3.26) and cannot resolve existence for the continuous slope problem.

5.4. Exact Periodic Families and Weak Limits

The periodic family in Proposition 4.6 can be evaluated explicitly. With $r_a = T/(gaH)$, introduce

$$m_e = \frac{H-a}{H-r_a}, \quad \kappa = \sqrt{\frac{3g(H-r_a)}{4T}}, \quad P(a) = \frac{2\mathrm{K}(m_e)}{\kappa},$$
$$h_\mu(x) = H - (H-a)\,\mathrm{sn}^2\left(\frac{\kappa(x-x_L)}{\mu}; m_e\right). \tag{5.4}$$

Here sn is the Jacobi elliptic function, with parameter m_e, and K is the complete elliptic integral of the first kind. Differentiating (5.4) recovers (4.18); the derivative is

$$h_{\mu'} = -\frac{2\kappa(H-a)}{\mu}\,\mathrm{sn}(\xi; m_e)\,\mathrm{cn}(\xi; m_e)\,\mathrm{dn}(\xi; m_e), \quad \xi = \frac{\kappa(x-x_L)}{\mu}.$$

Thus the depth and its derivative can be evaluated directly, including at the turning points, without spatial differencing.

Take $H = 1.2$, $T = 0.85^2$, $g = 9.81$, $I = [0, 60]$, and $n = 128, 256, 512, 1024, 2048$. For $a_n = H - 0.3/n$, choose $\mu_n = 60/(nP(a_n))$. The profile has a maximum at each endpoint and exactly n full periods. Its maximum error is $0.3/n$, while (4.19) gives total variation 0.6 for every n. **Figure 7** illustrates this uniform convergence with a nonzero variation defect.

A second family fixes $a = H - 0.08$ and uses the same integer-period choice of μ_n. Its total variation is $0.16n \asymp \mu_n^{-1}$, realizing the order of the upper bound (4.4). The period average is

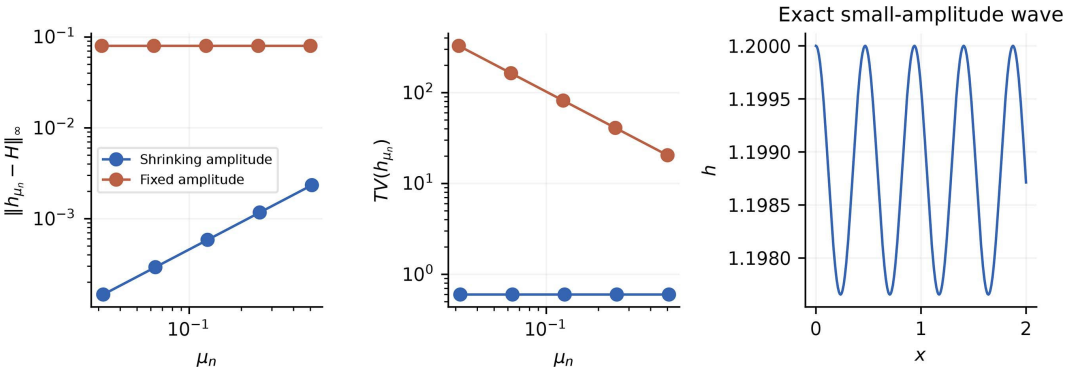


Figure 7. Exact stationary periodic families in a constant channel. Shrinking amplitude gives uniform convergence with total variation 0.6, whereas fixed amplitude gives total variation proportional to $1/\mu$. The right panel resolves the shrinking-amplitude wave for $n=128$.

$$\overline{h} = r_a + (H - r_a)\frac{\mathrm{E}(m_e)}{\mathrm{K}(m_e)}, \tag{5.5}$$

where E is the complete elliptic integral of the second kind. The complete oscillatory limit can also be computed from this exact family, including its nonlinear moments.

Proposition 5.1 (Young measure of a fixed-amplitude periodic family). *Fix* $0 < a < H$ *with* $r_a = T/(gaH) < a$, *and choose* $\mu_n = |I|/(nP(a))$ *in* (5.4). *Then, for every* $\Phi \in C([a,H])$,

$$\Phi(h_{\mu_n}) \overset{*}{\rightharpoonup} \int_a^H \Phi(z)\,\mathrm{dY}(z) \quad \text{in} \quad L^\infty(I), \tag{5.6}$$

where the probability measure, independent of x, *is*

$$\mathrm{dY}(z) = \frac{2}{P(a)}\sqrt{\frac{T}{3g}}\frac{\mathbf{1}_{(a,H)}(z)}{\sqrt{(H-z)(z-a)(z-r_a)}}\mathrm{d}z. \tag{5.7}$$

For $\varphi \in C^1(I)$ *the convergence satisfies*

$$\left|\int_I \left(\Phi(h_{\mu_n}) - \int_a^H \Phi \mathrm{dY}\right)\varphi \mathrm{d}x\right| \le C_\Phi \mu_n \left(\|\varphi\|_\infty + \|\varphi'\|_{L^1(I)}\right), \tag{5.8}$$

with C_Φ *independent of* n. *The mean depth is* (5.5); *the variance of* Y *is strictly positive. Hence the family does not converge strongly in* $L^1(I)$ *or* $L^2(I)$.

Proof. In the fast coordinate $y = (x - x_L)/\mu_n$, each depth $z \in (a,H)$ is visited twice per period. Equation (4.18) gives the residence density

$$\left|\frac{\mathrm{d}y}{\mathrm{d}z}\right| = \sqrt{\frac{T}{3g}}\frac{1}{\sqrt{(H-z)(z-a)(z-r_a)}}.$$

Division by $P(a)$ and summation over the two visits give (5.7). Its integral is one by the period formula. For each continuous Φ, subtract its period mean from the continuous periodic function of y obtained by composing Φ with the depth profile. The resulting zero-mean function has a bounded periodic primitive. Inte-

gration by parts in x gives (5.8). Density of $C^1(I)$ in $L^1(I)$ and boundedness of $\Phi(h_{\mu_n})$ prove (5.6) for all L^1 test functions. Taking $\Phi(z)=z$ recovers the mean in (5.5). The measure assigns positive mass to every subinterval of (a,H), so its variance is positive. The weak limit of the depth is its mean, whereas its second moment does not converge to the square of that mean. Strong L^2 convergence is therefore impossible. Uniform boundedness would upgrade strong L^1 convergence to strong L^2 convergence, so strong L^1 convergence is impossible as well. □

For the numerical illustration, the oscillatory integrals are evaluated against $\varphi(x)=\exp\left(-\left((x-30)/9\right)^2\right)$ and compared with (5.5). The exact family has endpoint depth H, but its weak mean lies strictly between a and H; it thus also illustrates that a weak limit need not retain that trace. This construction gives an explicit oscillatory limit in a constant channel. It does not identify the limit of the variable-channel hydraulic-jump-data computations.

6. Finite-Volume Profiles, Refinement and Boundary-Data Portraits

We now use the Gaussian geometry (2.18), the boundary states (3.26), and the discretization of Section 3.4. The equilibria solve (3.25) by the Newton procedure of Section 3.5. Their comparison with the hydrostatic references includes the effects of dispersion, spatial discretization and boundary realization. The continuous slope problem of Section 5 has a different geometry and boundary closure, as summarized in Table 2; the present computations are not a mesh-convergence test for that problem.

6.1. Discrete Norms and Hydrostatic Calibration

For a vector $e=(e_i)_{i=1}^N$, define

$$\|e\|_{p,N}=\left(\Delta x\sum_{i=1}^{N}|e_i|^p\right)^{1/p},\quad 1\le p<\infty,\quad \|e\|_{\infty,N}=\max_i|e_i|. \tag{6.1}$$

The sampled depth errors and total variation are

$$E_{p,N}=\left\|\left(h_i-h_0(x_i)\right)_{i=1}^N\right\|_{p,N},\quad \mathrm{TV}_N(h)=\sum_{i=1}^{N-1}|h_{i+1}-h_i|. \tag{6.2}$$

The norms are absolute spatial norms, without division by $|I|$. At a hydraulic jump, the reference is evaluated at cell centers. Moving the sampled jump by one cell changes $E_{1,N}$ by a quantity of order Δx, while the maximum error can remain comparable to the jump strength.

At $\mu=0$, all three data in Section 2.5 are computed on $N=80,160,320,640$ cells. From the coarsest to the finest mesh, the subcritical $E_{1,N}$ decreases from 0.196 to 0.0245, consistent with first-order spatial accuracy. The corresponding transcritical errors decrease from 0.233 to 0.0372, and the jump-data errors from 0.494 to 0.0753. For the jump data, $E_{\infty,N}$ remains about 0.33 because the numer-

ical transition is spread over several cells and displaced relative to the exact jump. Figure 8 provides this hydrostatic calibration before positive dispersion is introduced.

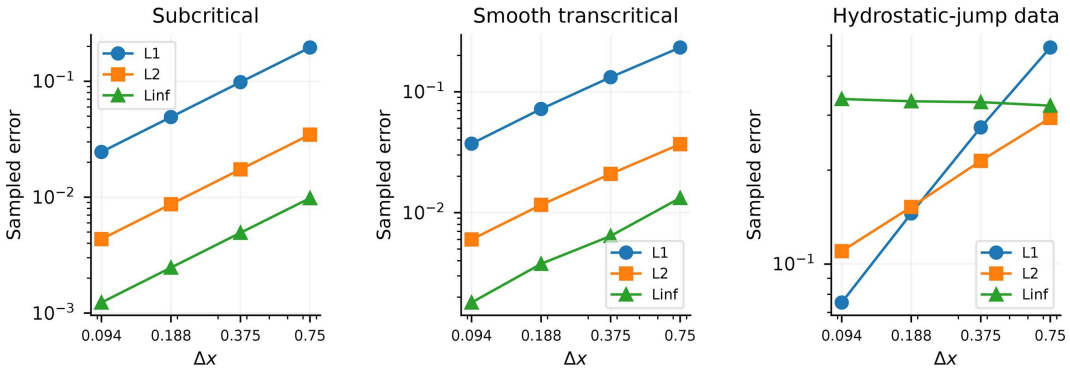


Figure 8. Hydrostatic finite-volume approximation, $\mu = 0$. The sampled L^1 and L^2 errors decrease under refinement for all three reference data. The maximum error across the hydraulic jump is affected by the position and numerical width of the transition.

6.2. Dispersive Profiles and Mesh Sensitivity

The same three data are computed at $\mu = 1, 1/2, 1/4$ and $N = 80, 160, 320, 640$. Figure 9 compares the finest profiles with their hydrostatic references, and Figure 10 gives their errors and total variations. The stationary mass equation makes the face mass flux constant to the nonlinear tolerance. Cell discharges remain unknowns of the coupled system, as specified after (3.25).

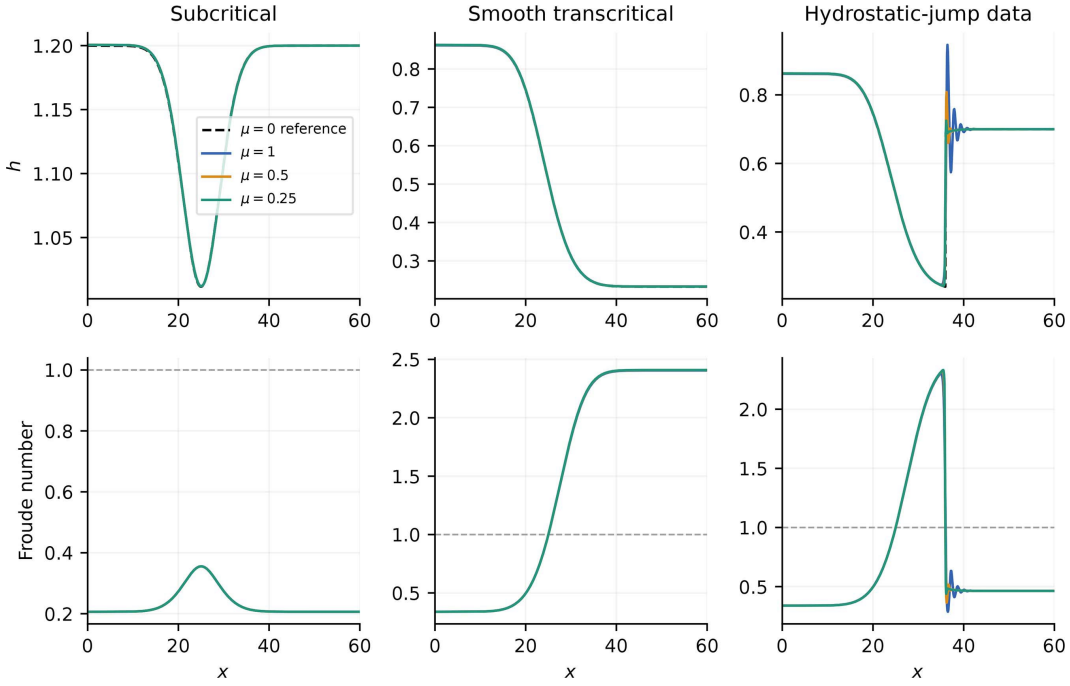


Figure 9. Finite-volume equilibria for the main pressure closure at $N = 640$ and $\mu = 1, 1/2, 1/4$. Black dashed curves are the hydrostatic references. Oscillatory transitions appear for the hydraulic-jump data.

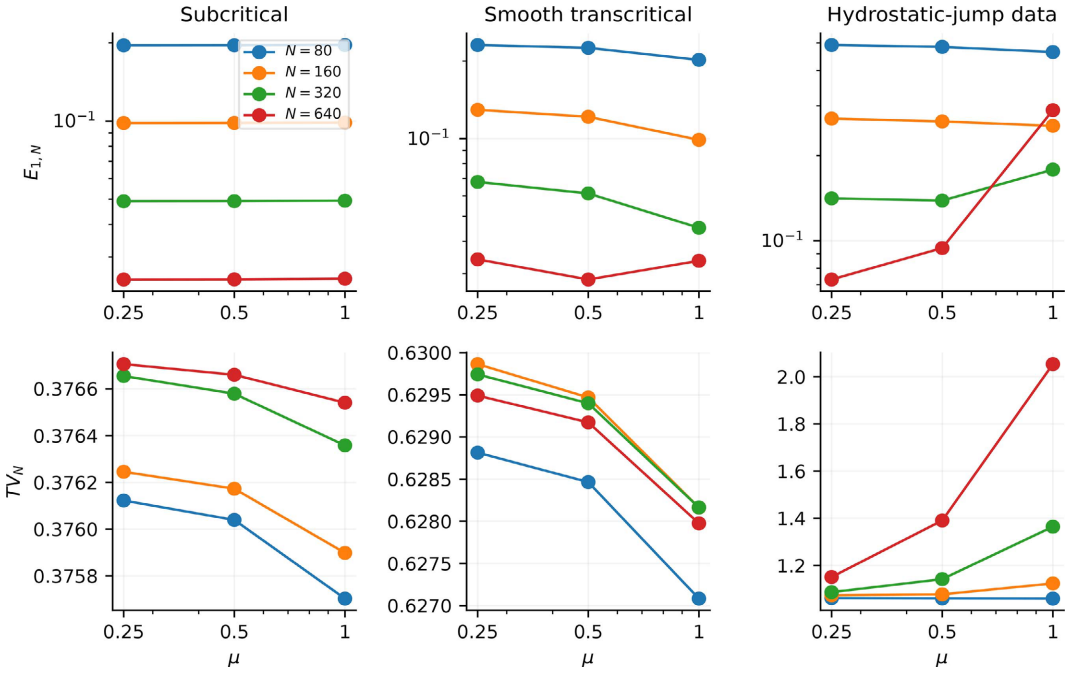


Figure 10. Depth errors and total variations as functions of μ at four fixed meshes. The curves reflect the combined effects of dispersion and spatial discretization.

For the subcritical data, the continuous dispersive correction at $\mu = 1$ has maximum size about 6.3×10^{-5} in Table 3. By comparison, the hydrostatic finite-volume error at $N = 640$ is about 1.2×10^{-3} in maximum norm. The geometries and boundary closures differ between these two calculations, but the scale comparison shows why the quadratic continuous correction is difficult to distinguish from spatial error on these finite-volume meshes.

For the jump data, refinement is extended to $N = 1280$ and 2560 at fixed positive dispersion. At $\mu = 1$, the total variation grows from 1.06 at $N = 80$ to 6.52 at $N = 2560$. For $N = 320, 640, 1280, 2560$, the respective L^1 distances to the hydrostatic jump are 0.179, 0.290, 0.616 and 1.259. The oscillatory region becomes more extensive, as shown in Figure 11, and successive fine-mesh profiles have not converged in maximum norm. These observations concern refinement at fixed μ; the variation divergence in Corollary 4.8 concerns a different limit and the continuous slope boundary problem.

The HLL flux (3.22) introduces numerical dissipation. Oscillations can therefore be damped when their wavelength is poorly resolved. Decreasing μ on a fixed mesh may produce a profile close to the hydrostatic transition even though Theorem 4.7 excludes a strong hydraulic-jump limit for continuous families under its hypotheses. Establishing a continuous small-dispersion limit would require first identifying the boundary problem approximated as $\Delta x \to 0$ at fixed $\mu > 0$, and then resolving that spatial limit at each dispersion scale. A small-μ limit on a fixed mesh is not interchangeable with this successive limiting procedure. Even resolution of the oscillation wavelength alone would not identify the continuous boundary conditions.

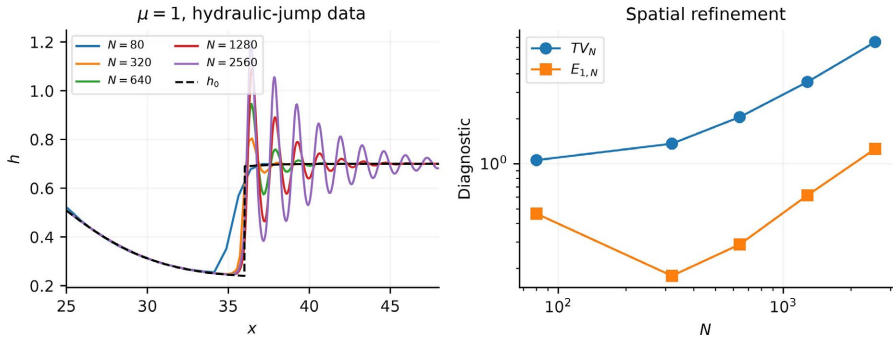


Figure 11. Refinement at fixed positive dispersion for the hydraulic-jump data. Increasing resolution reveals oscillations that are damped on coarser meshes; the finest displayed profiles remain sensitive to spatial resolution.

Two additional diagnostics measure cancellation and averaging of the oscillations. For $k=1,\cdots,4$, the signed cosine moments are

$$C_{k,N}=\Delta x\sum_{i=1}^{N}\left(h_i-h_0\left(x_i\right)\right)\cos\left(\frac{k\pi x_i}{60}\right). \tag{6.3}$$

For averaging widths $w=0.5,1,2$, let $m_w=\max\left(1,\text{round}\left(w/\Delta x\right)\right)$ and define

$$\left(\mathcal{A}_{m_w}h\right)_i=\frac{1}{m_w}\sum_{j=-\lfloor m_w/2\rfloor}^{\lceil m_w/2\rceil-1}h_{i+j},$$

extending the nearest endpoint value beyond the mesh. The smoothed discrepancy is $\left\|\mathcal{A}_{m_w}h-\mathcal{A}_{m_w}h_0\right\|_{1,N}$, with $\left(h_0\right)_i=h_0\left(x_i\right)$. These quantities describe cancellation at specified scales. Identifying a weak limit would require convergence under further refinement and a sufficiently rich set of test functions.

6.3. Construction and Classification of the Discrete Portrait

The portrait records branches reached by the specified continuation at a fixed mesh and exterior-state closure. It is not an exhaustive classification of discrete roots or of continuous stationary solutions. The axes retain the prescribed exterior data $\left(Q_L,h_R\right)$, which need not coincide with the attained face mass flux and outlet trace.

The portrait is computed at $\mu=1$ and $N=320$ on the parameter grid $Q=0.5+0.025j$, $j=0,\cdots,24$, and $h_R=0.15+0.02k$, $k=0,\cdots,55$, supplemented by the three outlet depths of Section 2.5. There are 25 discharge values and 59 distinct outlet depths. At each fixed discharge, the depths are visited in decreasing order.

The preceding accepted equilibrium at the same discharge supplies the first initial guess, with at most 25 Newton iterations and the stopping tolerance of Section 3.5. If that attempt fails, the solution is restarted on 40 cells and continued through $N=80,160,320$, allowing at most 45 Newton iterations per level. The initial 40-cell depth is selected as follows: use the subcritical hydrostatic profile when $h_R>H_{\text{sub}}\left(Q\right)$; use the controlled-jump profile when $H_{\text{conj}}\left(Q\right)<h_R<H_{\text{sub}}\left(Q\right)$;

otherwise use the smooth subcritical-to-supercritical profile (2.9) as an initial shape. In the last case the shape need not attain the target h_R; the target exterior datum is imposed throughout the nonlinear solve. For pairs still unresolved after the sweep, an available equilibrium of the material variant provides an additional initial guess, with at most 60 Newton iterations for the main closure.

A computed state enters the portrait only if

$$\min_i h_i > 0, \quad \|R(U)\|_\infty < 10^{-8}, \quad \|\mathcal{F}(U)\|_\infty < 10^{-8}, \tag{6.4}$$

with all face fluxes and the temporal inversion well defined. These tests select equilibria reached by the stated continuation procedure. Other initial guesses may reach other discrete branches.

Classification uses the cell Froude numbers $F_i = |Q_i/A_i| / \sqrt{g h_i}$, in the following order. A profile is subcritical when $\max_i F_i \le 1.001$. Otherwise it is assigned to the nearly supercritical class if $\min_i F_i \ge 0.999$. Among the remaining profiles, $F_1 < 1 < F_N$ identifies a subcritical inlet and supercritical outlet, while $F_1 < 1$ and $F_N < 1$ identify a mixed profile with subcritical endpoints. Any other endpoint configuration is kept as a separate class.

For a mixed profile with subcritical endpoints, the downstream return to criticality is the first pair with $x_i > 25$, $F_i > 1$ and $F_{i+1} \le 1$. Linear interpolation gives

$$x_t = x_i + \Delta x \frac{F_i - 1}{F_i - F_{i+1}}. \tag{6.5}$$

A return with $x_t > 60 - 4\Delta x = 59.25$ is placed in the last-four-cell class. These numerical thresholds specify the resolution at which the displayed regimes are distinguished.

Of the 1475 parameter pairs, 1473 satisfy (6.4): 567 are subcritical, 648 have a subcritical inlet and supercritical outlet, 225 have an interior downstream return, and 33 return within the last four cells. The unresolved pairs are $(0.775, 0.65)$ and $(0.9, 0.71)$. They indicate failure of the stated solution attempts, with existence and multiplicity at those parameters left undetermined.

Figure 12 compares the discrete classification with the hydrostatic envelopes of Section 2.3. Figure 13 gives the absolute outlet discrepancy $|h_N - h_R|$ on a logarithmic color scale. Its maximum value is approximately 0.256, demonstrating the effect of imposing h_R through an exterior state. The portrait therefore classifies the boundary problem of Section 3.4; a classification with the strong trace $h(x_R) = h_R$ requires the separate continuous formulation.

For comparisons between boundary closures, the outlet discrepancy should be supplemented by the inlet-flux discrepancy $|\hat{q}_N - Q_L|$, the cell-to-face discrepancy $\max_i |Q_i - \hat{q}_N|$, and one-sided depth slopes at the endpoints. These additional diagnostics are proposed for further computations; no values for them are reported here. Small stationary residuals alone do not establish small boundary discrepancies.

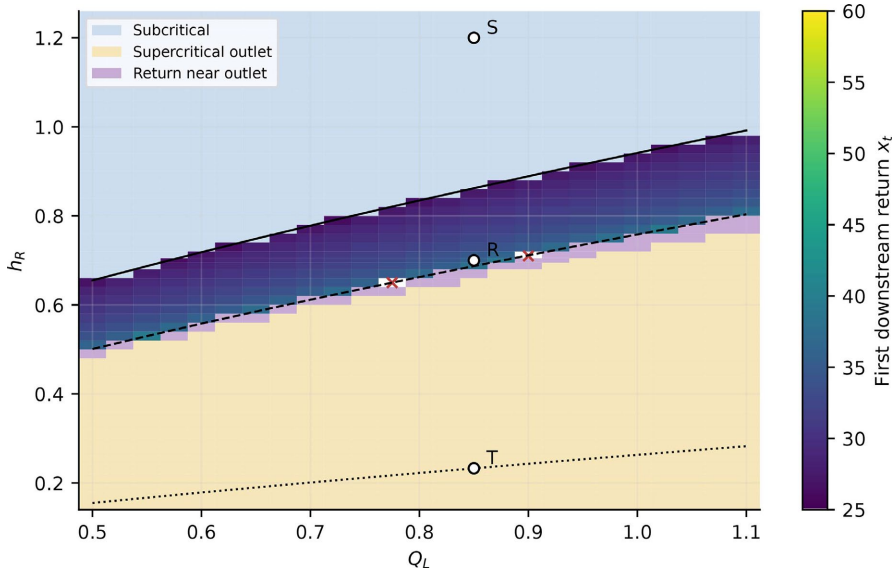


Figure 12. Discrete branches reached by the specified continuation for the main closure, $\mu = 1$ and $N = 320$. Axes are the exterior data (Q_L, h_R). The color scale gives the downstream critical return of a mixed profile. Black curves are hydrostatic reference envelopes; crosses mark unresolved attempts, not proven nonexistence. This is not an exhaustive continuous or discrete phase portrait.

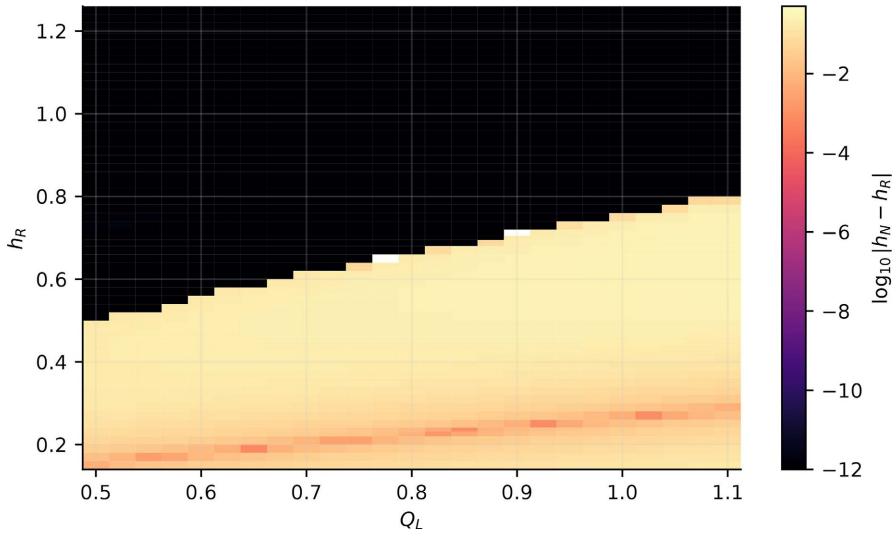


Figure 13. Attained outlet depth versus exterior depth for the same discrete portrait, at $\mu = 1$ and $N = 320$. Colors represent $\log_{10}\max\left(|h_N - h_R|, 10^{-12}\right)$. The largest absolute discrepancy is about 0.256. This measures the realization of the exterior-state condition (0.57), not an error in a strongly imposed continuous trace.

6.4. Sensitivity to the Pressure Closure

The variant defined in Section 3.3 is discretized by the replacements stated after (3.24), using the same fluxes, exterior states and nonlinear solution procedure. At $N = 640$ and $\mu = 1$, the maximum depth differences between W and M are approximately 7.94×10^{-6}, 2.15×10^{-4} and 2.36×10^{-2} for the subcritical, tran-

scritical and jump data, respectively. Figure 14 shows that the oscillatory transition is the most sensitive of the three configurations. The 36 comparisons with evolution from rest described in Section 7 are also performed for M; all satisfy the stationarity tests, with a maximum depth difference from the direct equilibrium below 2.12×10^{-8}.

The material-variant portrait accepts 1473 pairs on the same grid, with 567 subcritical profiles, 649 profiles with supercritical outlet, 225 interior returns and 32 last-four-cell returns. At $(Q,h_R)=(1.1,0.79)$, decreasing and increasing outlet-depth continuations also give two material-variant equilibria whose maximum depth difference is approximately 0.196, with stationary residuals below 4×10^{-14}. These observations concern discrete solutions at the stated mesh and closure. They motivate branch continuation in addition to a single parameter sweep when investigating multiplicity.

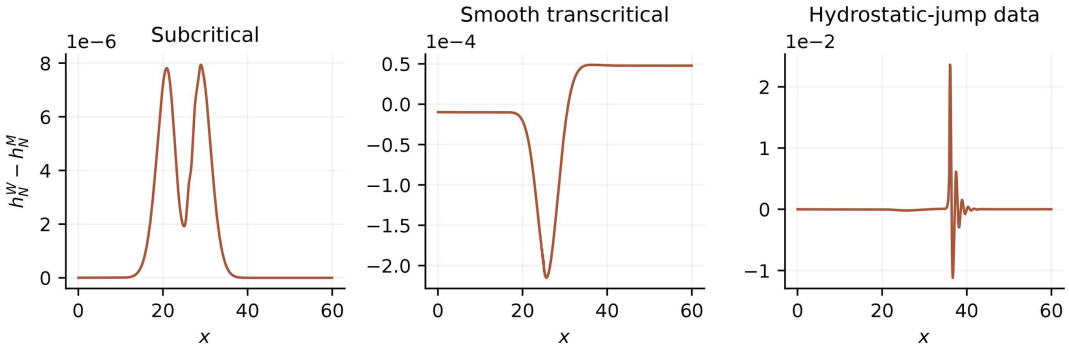


Figure 14. Depth differences between the width-weighted and material-derivative equilibria at $\mu=1$, $N=640$. The comparison isolates the width-dependent pressure terms identified in (3.19).

7. Verification of Discrete Equilibria by Evolution from Rest

The direct and temporal procedures of Sections 3.5 and 3.6 solve the same semidiscrete equations by different routes. We now test whether an evolution initialized at rest approaches the equilibrium obtained by Newton iteration. The comparison is performed at fixed mesh and boundary closure, so spatial refinement remains the separate question studied in Section 6.2.

7.1. Initialization, Time Steps and Stationarity Tests

For each reference datum, each $\mu\in\{0,1/4,1/2,1\}$ and each $N\in\{80,160,320\}$, prescribe the initial state

$$Q_i(0)=0,\quad \eta_i(0)=h_R+d(60),\quad A_i(0)=\sigma_i\left(h_R+d(60)-d_i\right). \tag{7.1}$$

All these depths are positive. The boundary states (3.26) are applied from the first stage, with the target discharge and outlet depth fixed throughout the evolution.

At each time step, use (3.37) with

$$\Delta t_n=\min\left\{\frac{0.45\Delta x}{\max_i\left(\left|u_i^n\right|+\sqrt{gh_i^n}\right)},3200-t_n\right\}. \tag{7.2}$$

Every stage recomputes the pressure coefficients and solves (3.36) at its own state. An invalid stage, including nonpositive area or a nonpositive reconstructed face depth, causes the entire step to be retried from U^n with half the time step. At most ten attempts are allowed, and a finite positive final state is required before advancing time. The choice (7.2) and these checks specify the computational protocol; a stability or positivity theorem for the full dispersive discretization is not assumed.

After the first step and subsequently at intervals of at least ten time units, let $U^{[m]}$ denote the current state and evaluate

$$\left\|\mathcal{F}\left(U^{[m]}\right)\right\|_\infty, \quad \left\|R\left(U^{[m]}\right)\right\|_\infty, \quad \left\|U^{[m]}-U^{[m-1]}\right\|_\infty. \tag{7.3}$$

Stationarity is accepted when all three quantities are below 10^{-8} at three consecutive checks. A failed check resets the count. Each evolution is allowed to reach $t=3200$ if the stationarity criterion has not been met earlier.

Denote the accepted temporal state by $\left(h^t,Q^t\right)$ and the direct equilibrium by $\left(h^s,Q^s\right)$. Their differences are evaluated with (6.1). Since the temporal initial state is (7.1), this test examines the evolution towards an equilibrium as well as the residual of that equilibrium.

7.2. Mass Balance and Time-Quadrature Checks

Summing the first equation of (3.25) makes all interior mass fluxes cancel. With $M^n=\Delta x\sum_i A_i^n$, the three-stage method therefore gives

$$M^{n+1}-M^n=\Delta t_n\sum_{j=0}^{2}\omega_j\left(\hat{F}_{A,L}^{(j)}-\hat{F}_{A,R}^{(j)}\right), \quad \left(\omega_0,\omega_1,\omega_2\right)=\left(\frac{1}{6},\frac{1}{6},\frac{2}{3}\right). \tag{7.4}$$

The fluxes are evaluated at $U^n,U^{(1)},U^{(2)}$, respectively. The accumulated mass discrepancy is the difference between M^n-M^0 and the sum of the right-hand side of (7.4) over accepted steps. It uses the boundary HLL fluxes determined by (3.26).

An analogous time-quadrature check compares the change in $\Delta x\sum_i Q_i$ with the sum of $\Delta t_n\Delta x\sum_j\omega_j\sum_i\mathcal{F}_{Q,i}\left(U^{(j)}\right)$. Here $U^{(0)}=U^n$, and $\mathcal{F}_Q$ includes the pressure inversion. This checks consistency of the temporal update with its evaluated right-hand side. Mechanical energy conservation is a different property, which is not implied by either quadrature check for the dissipative HLL discretization.

7.3. Comparison of Temporal and Direct Equilibria

All 36 evolutions satisfy (7.3). Across the three data, four dispersion values and three meshes, the largest maximum-norm difference between the temporal and direct states is 2.07×10^{-8} for depth and 1.47×10^{-8} for discharge. The largest final temporal and stationary residuals are below 8.5×10^{-10}, and the largest accumulated mass discrepancy is 4.70×10^{-11}. Repeating the jump-data calculation at $N=160$, $\mu=1$ with half the time step changes the final depth by

1.20×10^{-10} in maximum norm.

Table 5 gives the $N=320$ results. The labels S, T and R denote the subcritical, smooth transcritical and hydraulic-jump reference data, respectively. At $\mu=0$, the comparison is between the hydrostatic temporal evolution and its discrete equilibrium; its error relative to the exact hydrostatic profile was examined in Section 6.1. At positive dispersion, both states solve the finite-volume boundary problem specified in Section 3.4.

Table 5. Direct and temporal equilibria at $N=320$. Final time is the time at which the three consecutive stationarity checks have been satisfied. Norms are those of (6.1).

Data	μ	Final t	$\left\|h^t-h^s\right\|_{2,N}$	$\left\|h^t-h^s\right\|_{\infty,N}$	$\left\|Q^t-Q^s\right\|_{\infty,N}$
S	0	1772.5	1.84×10^{-8}	3.40×10^{-9}	1.23×10^{-9}
S	0.25	1772.5	1.84×10^{-8}	3.39×10^{-9}	1.16×10^{-9}
S	0.5	1772.6	1.84×10^{-8}	3.39×10^{-9}	9.87×10^{-10}
S	1	1772.5	1.84×10^{-8}	3.34×10^{-9}	6.34×10^{-10}
T	0	290.2	1.99×10^{-9}	3.88×10^{-10}	1.05×10^{-9}
T	0.25	290.2	1.98×10^{-9}	3.86×10^{-10}	1.04×10^{-9}
T	0.5	290.2	1.94×10^{-9}	3.78×10^{-10}	1.02×10^{-9}
T	1	290.4	1.80×10^{-9}	3.52×10^{-10}	9.56×10^{-10}
R	0	640.8	1.05×10^{-8}	1.98×10^{-8}	1.32×10^{-8}
R	0.25	640.7	1.12×10^{-8}	2.07×10^{-8}	1.47×10^{-8}
R	0.5	670.4	1.44×10^{-9}	2.47×10^{-9}	2.15×10^{-9}
R	1	660.5	6.88×10^{-9}	1.02×10^{-8}	9.28×10^{-9}

Figure 15 and Figure 16 compare the depth profiles at $\mu=0$ and $\mu=1$. Figure 17 shows the decay of the stationary residual during evolution from rest. The runs at $\mu=1/4$ and $\mu=1/2$ satisfy the same tests and are included in Table 5.

In every tested case, evolution from rest approaches the same discrete branch as the independently initialized Newton iteration. Together with the residual and time-step checks, this supports the direct computation of those equilibria. The two procedures share the spatial operator and boundary closure, so their agreement

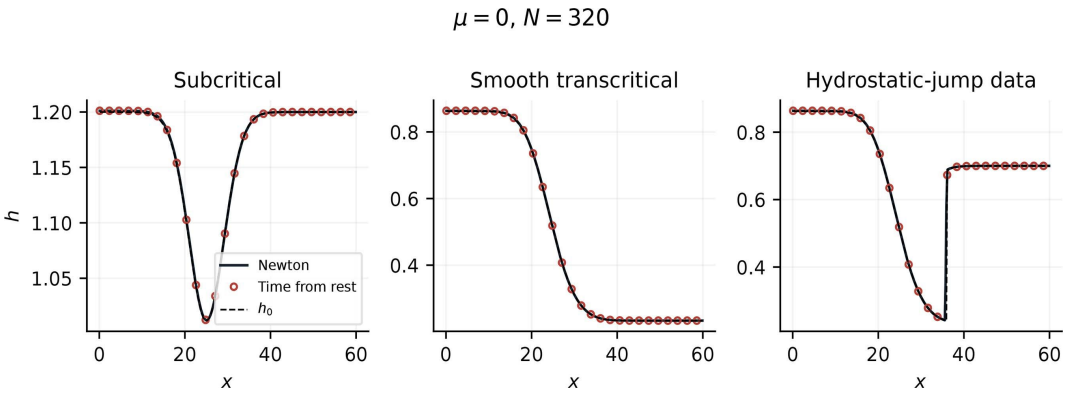


Figure 15. Hydrostatic model, $\mu=0$: direct equilibria and profiles reached by evolution from rest at $N=320$, compared with the exact hydrostatic references.

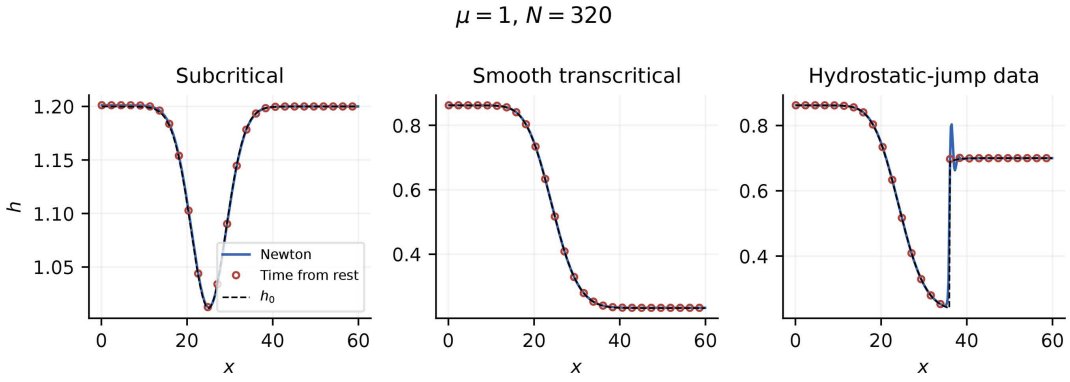


Figure 16. Dispersive model, $\mu = 1$: direct and temporal equilibria at $N = 320$. Agreement concerns this fixed spatial discretization; the jump-data refinement is shown separately in **Figure 11**.

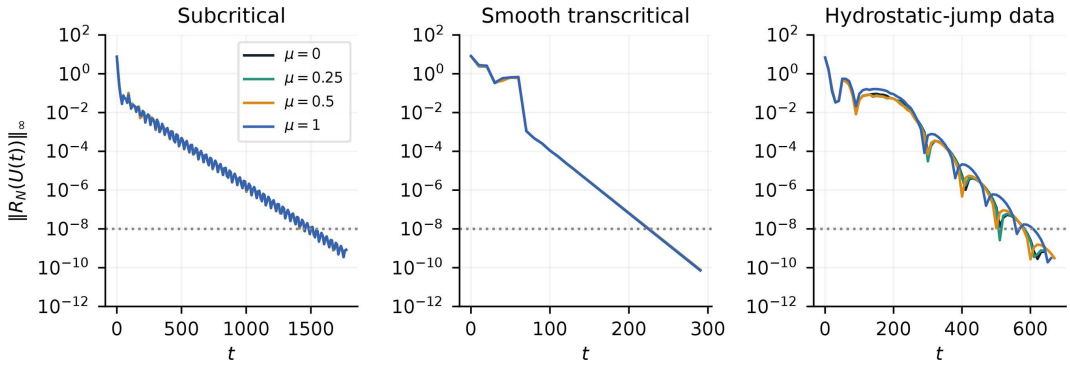


Figure 17. Stationary residual during evolution from rest at $N = 320$. The dotted line is the $10^{(-8)}$ threshold. Acceptance also requires the temporal residual and successive-state change in (7.3) to satisfy that threshold at three consecutive checks.

does not decide spatial consistency at the boundaries, uniqueness of other discrete branches, or nonlinear stability under arbitrary perturbations. The continuous slope problem and the resolution of fine oscillatory structures require their own analysis.

8. Conclusions

The hydrostatic construction gives an exact description of globally smooth stationary branches and of the controlled hydraulic-jump family. For the Gaussian geometry, the critical and conjugate-depth envelopes locate the unique jump within that family. This uniqueness does not classify stationary jumps with other upstream heads.

For the continuous dispersive slope problem, a non-resonant shooting argument proves local existence near uniform subcritical flow at fixed positive dispersion and small geometric perturbation. The small-dispersion comparison theorems concern existing families with the stated uniform depth, compactness and regime assumptions. Their stationary balances identify strongly convergent limits as continuous hydrostatic profiles of constant head. Uniform regularity away from criticality gives the quadratic estimate. A dissipative hydrostatic jump of nonzero

strength is excluded as a strong limit; for jump data with a uniformly subcritical outlet neighbourhood, total variation diverges if the required bounded family exists.

The oscillatory analysis distinguishes the variation defect of a strongly convergent depth from a nontrivial Young measure. Necessary averaged balances retain nonlinear moments and a nonnegative dispersive contribution. Exact periodic solutions in a constant channel provide an explicit measure and a quantitative weak-testing estimate. These results do not form a closed modulation theory or select the limit for hydraulic-jump data in a variable channel.

Continuous collocation and finite-volume computation address the two boundary problems specified in Table 2. The collocation failures for jump data leave existence unresolved. The finite-volume portraits record branches reached at a fixed mesh and closure. Agreement with evolution from rest verifies equilibria of the same discrete equations, while refinement and outlet diagnostics expose sensitivity to dissipation and boundary realization. Establishing the effective continuous boundary problem, continuing its stationary branches, and resolving the successive spatial and small-dispersion limits remain open tasks.

Acknowledgements

This work was supported by the ADEN-MED project (Adaptability to Extreme Events and Natural Risks—Application to the Mediterranean and Djibouti), funded by the Région Sud Provence-Alpes-Côte d'Azur under the AAP MEDCLIMAT "Natural Risks and Food Sovereignty"; the France 2030 Priority Research Program and Equipment (PEPR) Maths-Vives-Mathematics in Interactions, targeted project HYDRAUMATH (ANR-23-EXMA-007), operated by the French National Research Agency (ANR); the ANTARES project, funded by the ANR; and the PHAROS project (Monitoring Hydrodynamic Processes for Improved Adaptability to Oceanographic and Submergence Risks), funded by the Région Sud Provence-Alpes-Côte d'Azur under the AAP Océan et Mer.

Conflicts of Interest

The author declares no conflicts of interest regarding the publication of this paper.

References

[1] Delestre, O., Lucas, C., Ksinant, P., Darboux, F., Laguerre, C., Vo, T.N.T., *et al.* (2012) SWASHES: A Compilation of Shallow Water Analytic Solutions for Hydraulic and Environmental Studies. *International Journal for Numerical Methods in Fluids*, **72**, 269-300. https://doi.org/10.1002/fld.3741

[2] Serre, F. (1953) Contribution à l'étude des écoulements permanents et variables dans les canaux. *La Houille Blanche*, **39**, 830-872. https://doi.org/10.1051/lhb/1953058

[3] Green, A.E. and Naghdi, P.M. (1976) A Derivation of Equations for Wave Propagation in Water of Variable Depth. *Journal of Fluid Mechanics*, **78**, 237-246. https://doi.org/10.1017/s0022112076002425

[4] Debyaoui, M.A. and Ersoy, M. (2020) Generalised Serre-Green-Naghdi Equations for

Open Channel and for Natural River Hydraulics. *Asymptotic Analysis*, **124**, 343-369. https://doi.org/10.3233/asy-201647

[5] Debyaoui, M.A. and Ersoy, M. (2021) A Generalised Serre-Green-Naghdi Equations for Variable Rectangular Open Channel Hydraulics and Its Finite Volume Approximation. In: Muñoz-Ruiz, M.L., Parés, C. and Russo, G., Eds., *Recent Advances in Numerical Methods for Hyperbolic PDE Systems*, Springer, 251-268. https://doi.org/10.1007/978-3-030-72850-2_11

[6] El, G.A. and Hoefer, M.A. (2016) Dispersive Shock Waves and Modulation Theory. *Physica D: Nonlinear Phenomena*, **333**, 11-65. https://doi.org/10.1016/j.physd.2016.04.006

[7] Kalisch, H., Khorsand, Z. and Mitsotakis, D. (2016) Mechanical Balance Laws for Fully Nonlinear and Weakly Dispersive Water Waves. *Physica D: Nonlinear Phenomena*, **333**, 243-253. https://doi.org/10.1016/j.physd.2016.03.001

[8] Bolbot, D., Mitsotakis, D. and Tzavaras, A.E. (2024) Oscillatory and Regularized Shock Waves for a Modified Serre-Green-Naghdi System. *Studies in Applied Mathematics*, **153**, e12694. https://doi.org/10.1111/sapm.12694

[9] Audusse, E., Bouchut, F., Bristeau, M., Klein, R. and Perthame, B. (2004) A Fast and Stable Well-Balanced Scheme with Hydrostatic Reconstruction for Shallow Water Flows. *SIAM Journal on Scientific Computing*, **25**, 2050-2065. https://doi.org/10.1137/s1064827503431090

[10] Harten, A., Lax, P.D. and Leer, B.V. (1983) On Upstream Differencing and Godunov-Type Schemes for Hyperbolic Conservation Laws. *SIAM Review*, **25**, 35-61. https://doi.org/10.1137/1025002

[11] Gottlieb, S. and Shu, C. (1998) Total Variation Diminishing Runge-Kutta Schemes. *Mathematics of Computation*, **67**, 73-85. https://doi.org/10.1090/s0025-5718-98-00913-2

[12] Hungerbühler, N. (1997) A Refinement of Ball's Theorem on Young Measures. *New York Journal of Mathematics*, **3**, 48-53. https://nyjm.albany.edu/j/1997/3-3.pdf

[13] Ascher, U.M., Mattheij, R.M.M. and Russell, R.D. (1995) Numerical Solution of Boundary Value Problems for Ordinary Differential Equations. Society for Industrial and Applied Mathematics. https://doi.org/10.1137/1.9781611971231

Appendix A. Verification of the Discrete Balances and Linearizations

The checks below test the algebraic components of the finite-volume procedure before interpreting its spatial and temporal results. They use the operators already defined in Section 3.

A.1. Rest States and Uniform Flow

For a constant free-surface level η_0 with positive depth, set $Q_i = 0$ and $h_i = \eta_0 - d_i$. Choose compatible exterior data $Q_L = 0$ and $h_R = \eta_0 - d_N$. At each face, (3.21) gives equal reconstructed states and zero velocity, so the mass flux vanishes. Adding the appropriate correction (3.23) to the pressure flux gives $g\sigma_i h_i^2/2$ on each side of cell i. These two contributions cancel in its momentum residual. All stationary dispersive pressure terms vanish because $u = 0$. Thus the lake-at-rest state satisfies (3.25) exactly in exact arithmetic.

In a constant-width channel with a flat bed, a uniform positive depth and discharge likewise give identical face fluxes, zero geometric corrections and zero dispersive pressure. For $N = 80$, $\mu = 1$, the Gaussian rest state with $\eta_0 = 1.2$ gives a temporal residual below 3.25×10^{-15}. In the constant channel $\sigma = 1$, $d = 0$, the uniform state $h = 1.2$, $Q = 0.85$ gives a zero evaluated residual. The same results hold for both pressure closures considered in Section 3.3.

A.2. Temporal Matrix and Stationary Jacobian

At a fixed state U, let $\mathcal{P}_U(w)$ denote the dispersive force in brackets in (3.25), with the full pressures (3.34) evaluated at $u_t = w$. The assembled temporal matrix must satisfy, for every vector v,

$$E(U)v = v - \mu^2 \left\{ \mathcal{P}_U(v/A) - \mathcal{P}_U(0) \right\}. \tag{A.1}$$

This compares the matrix action with the direct affine dependence of the pressure force on u_t. On a 24-cell subcritical reference state at $\mu = 1$, using $v_i = \sin(x_i/4) + 0.15\cos(x_i/3)$, the maximum discrepancy is 2.23×10^{-16} or less for either closure.

For the stationary Jacobian, compare the grouped perturbations described in Section 3.5 with the column-by-column centered differences (3.32), using the same state and perturbation sizes. The two matrices have zero evaluated difference in this check. This verifies that the seven-cell dependence and the fourteen perturbation groups recover the intended finite-difference Jacobian.

These identities test the discrete balance, stencil assembly and temporal pressure inversion. The spatial errors, boundary effects and convergence of the nonlinear and temporal procedures are assessed separately in Sections 6 and 7.